

1 **Effects of three-dimensional electric field on saltation during dust**
2 **storms: An observational and numerical study**

3

4 Huan Zhang¹, You-He Zhou^{1,*}

5

6 ¹Department of Mechanics and Engineering Science, College of Civil Engineering and
7 Mechanics, Lanzhou University, Key Laboratory of Mechanics on Disaster and
8 Environment in Western China, The Ministry of Education of China, Lanzhou 730000,
9 PR China.

10

11 *Correspondence to: You-He Zhou (zhouyh@lzu.edu.cn)

12

1 **Abstract.** Particle triboelectric charging being ubiquitous in nature and industry,
2 potentially plays a key role in dust events, including the lifting and transport of sand
3 and dust particles. However, the properties of the electric field (E-field) and its
4 influences on saltation during dust storms remain obscure as the high complexity of
5 dust storms and the existing numerical studies mainly limited to one-dimensional (1-
6 D) E-field. Here, we quantify the effects of real three-dimensional (3-D) E-field on
7 saltation during dust storms, through a combination of field observations and
8 numerical modelling. The 3-D E-fields in the sub-meter layer from 0.05 to 0.7 m above
9 the ground during a dust storm are measured at the Qingtu Lake Observation Array
10 site. The time-varying means of E-field series over a certain timescale are extracted by
11 the discrete wavelet transform and ensemble empirical mode decomposition methods.
12 The measured results show that each component of the 3-D E-field data roughly
13 collapses on a single 3-order polynomial curve when normalized. Such 3-D E-field data
14 close to the ground within a few centimeters has never been reported and formulated
15 before. Using the discrete element method, we then develop a comprehensive
16 saltation model, in which the triboelectric charging between particle-particle midair
17 collisions is explicitly accounted for, allowing us to evaluate the triboelectric charging
18 in saltation during dust storms properly. By combining the results of measurements
19 and modelling, we find that although the vertical component of the E-field (i.e. 1-D E-
20 field) inhibits sand transport, 3-D E-field enhances sand transport substantially.
21 Furthermore, the model predicts that 3-D E-field enhances the total mass flux and
22 saltation height by up to 20 % and 15 %, respectively. This suggests that a 3-D E-field
23 consideration is necessary if one is to explain precisely how the E-field affects saltation
24 during dust storms. These results further improve our understanding of particle
25 triboelectric charging in saltation and help to provide more accurate characterizations
26 of sand and dust transport during dust storms.

27
28
29

1 **1. Introduction**

2 Contact or triboelectric charging is ubiquitous in dust events (Harrison et al., 2016;
3 Kok and Renno, 2008; Lacks and Sankaran, 2011; Schmidt et al., 1998; Zheng et al.,
4 2003). The pioneering electric field (E-field) measurements in dust storms by W. A.
5 Douglas Rudge showed that the vertical atmospheric E-field was substantially
6 increased to 5-10 kV m⁻¹ and its direction reversed (became upward-pointing) during
7 a severe dust storm (Rudge, 1913). Later measurements in dust storms found
8 downward-pointing (Esposito et al., 2016), upward-pointing (Bo and Zheng, 2013; Yair
9 et al., 2016; Zhang and Zheng, 2018), and even alternating vertical E-field which
10 continually reverses direction (Kamra, 1972; Williams et al., 2009), with the magnitude
11 of up to ~100 kV m⁻¹.

12 The significant influences of E-field on pure saltation (that is, in the absence of
13 suspended dust/aerosol particles) have been verified, both numerically (e.g. Kok and
14 Renno, 2008; Zhang et al., 2014) and experimentally (e.g. Esposito et al., 2016;
15 Rasmussen et al., 2009). The effects of E-field on saltation during dust storms, however,
16 remain obscure. A clear difference between the numerical simulation and field
17 measurement is that: numerical simulation of pure saltation showed a reduction in
18 saltation mass flux by E-field (e.g. Kok and Renno, 2008; Zheng et al., 2003), whereas
19 recent field measurements found a dramatic increase in dust concentration during
20 dust storms (up to a factor of 10) by E-field (Esposito et al., 2016), suggesting that E-
21 field might enhance saltation mass flux during dust storms. This is probably because
22 only the vertical component of the E-field (i.e. 1-D) should be considered in pure
23 saltation, but there also in fact exist streamwise and spanwise components of E-field
24 in dust events. For example, Jackson and Farrell (2006) recorded the horizontal
25 component of the E-field of up to 120 kV m⁻¹ in dust devils. Zhang and Zheng (2018)
26 also found the streamwise and spanwise components (termed horizontal component)
27 of the E-field of up to 150 kV m⁻¹ in dust storms. Hence, E-field is actually three-
28 dimensional (3-D) during dust storms. In many cases, the magnitude of the horizontal
29 component is larger than that of the vertical component (Bo and Zheng, 2013; Zhang

1 and Zheng, 2018). The horizontal component should therefore not be neglected when
2 evaluating the role of E-field in saltation during dust storms.

3 Most field observations, such as Schmidt et al. (1998) and Bo et al. (2014), have
4 studied the electrical properties of sand particles in dust events. However, many
5 environmental (lurking) factors, such as relative humidity, soil moisture, surface crust,
6 etc., cannot be fully controllable (recorded) in these field observations. The
7 uncertainties in the field observations provide motivation for numerical studies of the
8 particle triboelectric charging in saltation. In addition, unlike pure saltation, the dust
9 storm is a very complex dusty phenomenon that is made up by numerous polydisperse
10 particles embedded in a high Reynolds-number turbulent flow. Such high complexity
11 of dust storms challenges the accurate simulation of 3-D E-field in dust storms. It is
12 therefore more straightforward to characterize 3-D E-field experimentally.

13 In this study, we evaluate the effects of 3-D E-field on saltation during dust storms
14 by combining measurements and modelling. To reveal the properties of 3-D E-field, we
15 simultaneously measured the 3-D E-fields in the sub-meter layer from 0.05 to 0.7 m
16 above the ground during a dust storm. Such a vertical profile of the 3-D E-field in the
17 sub-meter layer has not been previously characterized. To reveal how 3-D E-field
18 affects saltation during dust storms, we develop a comprehensive numerical model of
19 particle triboelectric charging in saltation. In this model, the charge transfers between
20 contacting particles are explicitly calculated, but the 3-D E-field is formulated directly
21 based on the data measured in our measurements, due to its huge challenges in
22 modelling. The effects of various important parameters, such as the density of charged
23 species and the height-averaged time-varying mean of the 3-D E-field, are also
24 investigated and described herein.

25 26 **2. Field campaign**

27 **2.1 Observational set-up and uncertainty**

28 We performed 3-D E-field measurements at the Qingtu Lake Observation Array
29 (QLOA) site (approximately $39^{\circ}12'27''$ N, $103^{\circ}40'03''$ E, as shown in Fig. 1a), in

1 May 2014. The measured physical quantities include: wind velocities at four heights
2 measured by the sonic anemometers (CSAT3B, Campbell Scientific, Inc.) with 50 Hz
3 sampling frequency; the number of saltating particles passing through the
4 measurement area (2 mm×25 mm) per second at six heights measured by sand particle
5 counter (SPC-91, Niigata Electric Co., Ltd.) with 1 Hz sampling frequency, thus providing
6 an estimation of the size distribution of saltating particles, saltation mass flux, and
7 saltation height (Text S1 in the Supplement); 3-D E-field at five heights measured by
8 the vibrating-reed E-field mill (VREFM, developed by Lanzhou University) with 1 Hz
9 sampling frequency. The layout of all instruments is shown in Fig. 1b. All instruments
10 are powered by solar panels.

11 A detailed description of VREFM can be found in the Supplement of Zhang et al.
12 (2017), but we describe it here briefly. The working principle of VREFM is based on the
13 dynamic capacity technique, as illustrated in the inset of Fig. 1b. Unlike traditional
14 atmospheric electric field mill, VREFM is composed of only one vibrating electrode. As
15 the electrode oscillates, it charges and discharges periodically. The magnitude of the
16 induced electric current $i(t)$ is proportional to the ambient E-field intensity E
17 (Zhang et al., 2017), i.e.

18

$$19 \quad i(t) \propto E\omega \cos(\omega t) \quad (1)$$

20

21 where ω is the vibration frequency of the electrode. The induced electric current is
22 then converted to an output voltage signal, which is linearly proportional to the
23 ambient E-field, through functional modules within VREFM. In addition, the length and
24 diameter of the VREFM sensor are approximately 2.5 cm and 7 cm, respectively. This
25 small size sensor allows us to measure E-field very close to ground but does not disturb
26 the ambient E-field significantly.

27 The measurement uncertainties in our field campaign are threefold: wind velocity
28 (CSAT3B), particle mass flux (SPC-91), and E-field (VREFM). The CSAT3B is factory
29 calibrated with an accuracy of $\pm 8 \text{ cm s}^{-1}$. And the SPC-91 is factory calibrated by a set

1 of filamentation wires of equivalent diameters from 0.138 to 0.451 mm, with an
2 uncertainty of ± 0.015 mm. The VREFM used in the field measurements is carefully
3 calibrated and selected in our lab by a parallel-plate E-field calibrator (Zhang et al.,
4 2017), and its maximum uncertainties range from $\sim 1.38\%$ to $\sim 2.24\%$ (see Text S2 in
5 the Supplement).

6

7 **2.2 Data analysis**

8 In general, the actual wind direction exits a specific angle from the prevailing wind
9 direction. A projection step is therefore needed to obtain the streamwise E-field, E_1 ,
10 and spanwise E-field, E_2 . For example, E_1 is equal to the sum of the projection of the
11 measured E_x and E_y (E-field in the direction of x and y axes, as shown in Fig. 1b)
12 to the streamwise wind direction.

13 After completing the projection step, we then perform the following steps
14 sequentially to reveal the pattern of 3-D E-field in the sub-meter layer: (1) estimating
15 time-varying mean values of E-field; (2) computing height-averaged time-varying mean
16 in the measurement region from 0.05 to 0.7 m above the ground; (3) normalizing E-
17 field by height-averaged mean values; and (4) finally fitting the vertical profiles of
18 normalized E-field by the 3-order polynomial functions. It is worth noting that the
19 measured time series in dust storms are generally non-stationary when viewed as a
20 whole (e.g. Zhang and Zheng, 2018). In such cases, the statistical values are time-
21 varying. Here, we use the discrete wavelet transform (DWT) method (Daubechies,
22 1990) and the ensemble empirical mode decomposition (EEMD) method (Wu and
23 Huang, 2009), which are widely used in various geophysical studies (e.g. Grinsted et
24 al., 2004; Huang and Wu, 2008; Wu et al., 2011), to estimate the time-varying mean
25 values of the measured non-stationary 3-D E-field data. We select these two methods
26 since the DWT with higher orders of Daubechies wavelet (e.g. db10) and the EEMD can
27 extract a reasonable and physically meaningful time-varying mean (Su et al., 2015).
28 Each step for revealing the 3-D E-field pattern is described in detail as follows:

29 The DWT uses a set of mutually orthogonal wavelet basis functions, which are

1 dilated, translated and scaled versions of a mother wavelet, to decompose an E-field
2 series E into a series of successive octave band components (Percival and Walden,
3 2000), i.e.,

$$4 \quad E = \sum_{i=1}^N \psi_i + \chi_N \quad (2)$$

6
7 Where N is the total number of decomposition levels, ψ_i denotes the i -th level
8 wavelet detail component, and χ_N represents the N -th level wavelet approximation
9 (or smooth) component. As N increases, the frequency contents become lower, and
10 thus the N -th level approximation component could be regarded as the time-varying
11 mean values (e.g. Percival and Walden, 2000; Su et al., 2015). In this study, the DWT
12 decomposition is performed with the Daubechies wavelet of order 10 (db10) at level
13 10, and thus the 10-th order approximation component can be defined as the time-
14 varying mean:

$$15 \quad \bar{E} = \chi_{10} \quad (3)$$

17
18 which reflect the averages of the E series over a scale of 2^{10} s (Percival and Walden,
19 2000).

20 On the other hand, according to the empirical mode decomposition (EMD)
21 method, the time series E can be decomposed as (Huang et al., 1998)

$$22 \quad E = \sum_{i=1}^N \xi_i + \eta_N \quad (4)$$

24
25 through a sifting process, where ξ_i are the intrinsic mode functions (IMFs), and η_N
26 is a residual (which is the overall trend or mean). To reduce the end effects and mode
27 mixing in EMD, the EEMD method is proposed by Wu and Huang (2009). In EEMD, a

1 set of white noise series, w_j ($j = 1, 2, \dots, N_e$), are added to the original signal E . Then,
 2 each noise-added series is decomposed into IMFs followed by the same sifting process
 3 as in EMD. Finally, the i -th EEMD component is defined as the ensemble mean of the
 4 i -th IMFs of the total of N_e noise-added series (see Wu and Huang, 2009 for details).

5 In this study, the time-varying mean values \bar{E} can be alternatively defined as the
 6 sum of the last four EEMD components, ξ_{10} to ξ_{13} , and the residual, η_{13} , i.e.

7

$$8 \quad \bar{E} = \sum_{i=10}^{13} \xi_i + \eta_{13} \quad (5)$$

9

10 According to the above definitions, the time-varying mean can be synchronously
 11 obtained by the DWT and EEMD methods. As an example, Fig. 2 shows the results of
 12 DWT analysis (Fig. 2b) and EEMD decompositions (Fig. 2c) for an E-field time series E
 13 in our field campaign. It can be seen that DWT and EEMD can properly capture a similar
 14 time-varying mean (Fig. 2a). This is because the EEMD is conceptually very similar to
 15 the DWT and thus behaves as a “wavelet-like” filter bank (Flandrin, 2004). As shown in
 16 Fig. 3, the frequencies contained in the DWT and EEMD components become
 17 progressively lower, where the mean frequencies of ψ_{10} and ξ_9 are 7.69×10^{-4} and
 18 7.24×10^{-4} Hz, respectively. The time-varying means (defined as the summation of the
 19 components below the dashed line in Fig. 3) χ_{10} and $\sum_{i=10}^{13} \xi_i + \eta_{13}$ show very close
 20 mean frequencies of 7.71×10^{-6} and 7.85×10^{-6} Hz, respectively. We thus conclude that
 21 such definitions in Eq. (3) and (5) can extract the time-varying mean over a certain
 22 scale of about 7.47×10^{-4} Hz (below the dashed line in Fig. 3).

23 Since the 3-D E-field are measured at five heights in our field campaign, we thus
 24 define the height-averaged time-varying mean values as

25

$$26 \quad \langle \bar{E}_i \rangle = \left| \frac{1}{(0.7 - 0.05)} \int_{0.05}^{0.7} \bar{E}_i dz \right| \quad (6)$$

27

1 in the range of 0.05 to 0.7 m height, in order to normalize the E-field data by a unified
2 quantity. Further, the E-field data can be normalized as

3

$$4 \quad E_i^* = \frac{E_i}{\langle E_i \rangle} \quad (7)$$

5

6 Additionally, to obtain the dimensionless vertical profile of 3-D E-field, the height z
7 should also be a dimensionless parameter. Here, the dimensionless height z^* is
8 defined as the ratio of height z to the mean saltation height \bar{z}_{salt} during the whole
9 observed dust storm, i.e.

10

$$11 \quad z^* = \frac{z}{\bar{z}_{salt}} \quad (8)$$

12

13 where the saltation height z_{salt} during a certain time interval is defined as the height
14 below which 99 % of the total mass flux is present and can be estimated based on the
15 measured SPC-91 data (see Text S1 in the Supplement for more details).

16 Finally, the dimensionless vertical profiles of 3-D E-field at different periods are
17 together fitted by the 3-order polynomial functions:

18

$$19 \quad E_i^*(z^*) = a_{0,i} + a_{1,i}z^* + a_{2,i}(z^*)^2 + a_{3,i}(z^*)^3, \quad i = 1,2,3 \quad (9)$$

20

21 where $i = 1, 2,$ and 3 correspond to the streamwise, spanwise, and vertical
22 components, respectively.

23

24 **3. Saltation model**

25 For modelling steady-state saltation, there are four primary processes, including
26 (1) particle saltating motion, (2) particle-particle midair collisions, (3) particle-bed
27 collisions, and (4) particle-wind momentum coupling (Dupont et al., 2013; Kok and
28 Renno, 2009). Also, the changes in both momentum and electrical charge of each

1 particle are taken into account in the particle-particle midair and particle-bed collisions.
 2 To avoid overestimating midair collisions in 2-D simulation (Carneiro et al., 2013), we
 3 simulate saltation trajectories in a real 3-D domain. We use the discrete element
 4 method (DEM), which explicitly simulates each particle motion and describes the
 5 collisional forces between colliding particles encompassing normal and tangential
 6 components, to advance the evaluation of the effects of particle midair collisions. In
 7 the following subsections, we will describe each process in detail.

8

9 **3.1 Size distribution of particle sample**

10 Granular materials in natural phenomena, such as sand, aerosols, pulverized
 11 material, seeds of crops, etc., are made up of discrete particles with a wide range of
 12 sizes ranging from a few micrometers to millimeters. The log-normal distribution is
 13 generally used to approximate the size distribution of the sand sample (Dupont et al.,
 14 2013; Marticorena and Bergametti, 1995). Thus, the mass distribution function of a
 15 sand sample with two parameters, average diameter d_m , and geometric standard
 16 deviation σ_p , can be written as

17

$$18 \quad \frac{dM(d_p)}{d\ln(d_p)} = \frac{1}{\sqrt{2\pi}\ln(\sigma_p)} \exp\left\{-\frac{[\ln(d_p) - \ln(d_m)]^2}{2[\ln(\sigma_p)]^2}\right\} \quad (10)$$

19

20 **3.2 Equations of saltating particles motion**

21 The total force acting on a saltating particle consists of three distinct interactions
 22 (Minier, 2016). The first one refers to the wind-particle interaction, which is dominated
 23 by the drag force with lifting forces such as Saffman force and Magnus force being of
 24 secondary importance (Dupont et al., 2013; Kok and Renno, 2009). The second
 25 interaction refers to the particle-particle collisional forces or cohesion caused by
 26 physical contact between particles. Such interparticle collisional forces can be
 27 described as a function of the overlaps between the colliding particles. The third
 28 interaction refers to the forces due to external fields such as gravity and E-field. In this

1 study, in addition to the drag force, we also take into account the Magnus force
 2 because of the remarkable rotation of saltating particles on the order of 100-1000 rev
 3 s⁻¹ (Xie et al., 2007). The effects of electrostatic forces on particle motion, which are
 4 significant for large wind velocity (Schmidt et al., 1998; Zheng et al., 2003), are also
 5 taken into account. Consequently, the full governing equations of saltating particles
 6 can be written as

$$8 \quad m_{p,i} \frac{d\vec{u}_{p,i}}{dt} = \vec{F}_i^d + \vec{F}_i^m + \sum_j (\vec{F}_{ij}^n + \vec{F}_{ij}^t) + m_i \vec{g} + \zeta_{p,i} \vec{E} \quad (11a)$$

$$9 \quad I_i \frac{d\vec{\omega}_{p,i}}{dt} = \vec{M}_i^{w-p} + \sum_j (\vec{M}_{ij}^c + \vec{M}_{ij}^r) \quad (11b)$$

10
 11 where $m_{p,i}$ is the mass of the i -th particle; $\vec{u}_{p,i}$ is the velocity of the particle; \vec{F}_i^d is
 12 the drag force; \vec{F}_i^m is the Magnus force; \vec{F}_{ij}^d and \vec{F}_{ij}^t are the normal and tangential
 13 collisional forces from the j -th particle, respectively; \vec{g} is the gravitational
 14 acceleration; $\zeta_{p,i}$ is the charge-to-mass ratio of the sand particles and is altered
 15 during every collision (see section 3.4); \vec{E} is the 3-D E-field given by our
 16 measurements; I_i is the moment of inertia; $\vec{\omega}_{p,i}$ is the angular velocity of the
 17 particle; \vec{M}_i^{w-p} is the torque caused by the wind on the particle; \vec{M}_{ij}^c and \vec{M}_{ij}^r are
 18 the tangential torque due to the tangential component of the particle collisional forces
 19 and the rolling resistance torque, respectively. The summation Σ represents
 20 considering all particles that are in contact with the i -th particle.

22 **3.2.1 Wind-particle interactions**

23 In the absence of saltating particles, the mean wind profile over a flat and
 24 homogeneous surface is well approximated by the log-law (Anderson and Haff, 1988)

$$26 \quad u_m(z) = \frac{u_*}{\kappa} \ln \frac{z}{z_0} \quad (12)$$

1

2 where u_m is the mean streamwise wind speed; z is the height above the surface;
 3 u_* is the friction velocity; $\kappa \approx 0.41$ is the von Kármán constant; z_0 is the
 4 aerodynamic roughness, which varies substantially form different flow conditions and
 5 can be approximately estimated as $d_m/30$ for the aeolian saltation on Earth (e.g.
 6 Carneiro et al., 2013; Kok et al., 2012). In the presence of saltation, due to the
 7 momentum coupling between the saltating particles and wind flow, the modified wind
 8 speed gradient can be written as follows for steady-state and horizontally-
 9 homogeneous saltation (e.g. Kok and Renno, 2009; Pähtz et al., 2015)

10

$$11 \quad \frac{du_m(z)}{dz} = \frac{u_*}{\kappa z} \sqrt{1 - \frac{\tau_p(z)}{\rho_a u_*^2}} \quad (13)$$

12

13 where ρ_a is the air density, $\tau_p(z)$ is the particle momentum flux and can be
 14 numerically determined by (Carneiro et al., 2013; Shao, 2008)

15

$$16 \quad \tau_p(z) = -\frac{\sum m_{p,i} u_{p,i} w_{p,i}}{L_x L_y \Delta z} \quad (14)$$

17

18 with L_x , L_y , and Δz being the streamwise-, spanwise-width of the computational
 19 domain, and vertical grid size, respectively; $u_{p,i}$ and $w_{p,i}$ are the streamwise and
 20 vertical components of particle velocity. The summation in Eq. (14) is performed on
 21 the particles located in the range of $[z, z + \Delta z]$. Once saltating particle trajectories are
 22 known, the wind profile can be determined through integrating Eq. (13) with the no-
 23 slip boundary condition $u_m = 0$ at $z = z_0$.

24

25 Since sand particles are much heavier than the air and are well smaller than the
 26 Kolmogorov scales, the drag force is the dominant force affecting particle motion,
 27 which is expressed by (Anderson and Haff, 1991)

27

$$\vec{F}_i^d = -\frac{\pi d_p^2}{8} \rho_a C_d \vec{u}_r |\vec{u}_r| \quad (15)$$

where d_p is the diameter of the particle; C_d is the drag coefficient; and $\vec{u}_r = \vec{u}_p - \vec{u}_w$ is the particle-to-wind relative velocity. The drag coefficient C_d is a function of the particle Reynolds number, $Re_p = \rho_a |\vec{u}_r| d_p / \mu$, where μ is the dynamic viscosity of the air. We calculate the drag coefficient by an empirical relation $C_d = \left[(32/Re_p)^{2/3} + 1 \right]^{3/2}$, which is applicable to the regimes from Stokes flow $Re_p \ll 1$ to high Reynolds number turbulent flow (Cheng, 1997).

Additionally, we also account for the effects of particle rotation on particle motion using the Magnus force expressed as (Anderson and Hallet, 1986; Loth, 2008; White and Schulz, 1977)

$$\vec{F}_i^m = \frac{\pi d_p^2}{8} \rho_a C_m (\vec{\omega}_{p,i} \times \vec{u}_r) \quad (16)$$

where C_m is a normalized spin lift coefficient depended on the particle Reynolds number and the circumferential speed of the particle. The torque acting on a particle caused by wind flow is calculated from (Anderson and Hallet, 1986; Kok and Renno, 2009; Shao, 2008)

$$\vec{M}_i^{w-p} = \pi \mu d_i^3 \left(\frac{1}{2} \frac{du_m}{dz} - \vec{\omega}_i \right) \quad (17)$$

3.2.2 Particle-particle midair collisions

Under moderate conditions, saltation is a dilute flow in which the particle-particle collisions are negligible. However, as wind velocity increases, midair collisions become increasingly pronounced, especially in the near-surface region (Sørensen and McEwan, 1996). Previous studies found that the probability of mid-air collisions of saltating particles almost increased linearly with wind speed (Huang et al., 2007) and such collisions indeed enhanced the total mass flux substantially (Carneiro et al., 2013). For

1 spherical particles, one of the most commonly-used collisional force models is the
 2 nonlinear viscoelastic model, consisting of two components, i.e. elastic and viscous
 3 forces (Brilliantov et al., 1996; Haff and Anderson, 1993; Silbert et al., 2001; Tuley et
 4 al., 2010).

5 Considering two spherical particles i and j with diameters d_i and d_j , and
 6 position vectors \vec{x}_i and \vec{x}_j , are in contact with each other. The relative velocity \vec{v}_{ij}
 7 at the contact point and its normal and tangential components, \vec{v}_{ij}^n and \vec{v}_{ij}^t , are
 8 respectively defined as (Norouzi et al., 2016; Silbert et al., 2001)

$$10 \quad \vec{v}_{ij} = \vec{u}_{p,i} - \vec{u}_{p,j} + 0.5(d_i\vec{\omega}_{p,i} + d_j\vec{\omega}_{p,j}) \times \vec{n}_{ij} \quad (18a)$$

$$11 \quad \vec{v}_{ij}^n = (\vec{v}_{ij} \cdot \vec{n}_{ij})\vec{n}_{ij} \quad (18b)$$

$$12 \quad \vec{v}_{ij}^t = \vec{v}_{ij} - \vec{v}_{ij}^n \quad (18c)$$

13
 14 where $\vec{n}_{ij} = (\vec{x}_j - \vec{x}_i)/|\vec{x}_j - \vec{x}_i|$ is the unit vector in the direction from the center
 15 of particle i point toward the center of particle j . Suppose that these colliding
 16 particles having identical mechanical properties with Young's modulus Y , shear
 17 modulus G , and Poisson's ratio ν , and thus the normal collisional force can be
 18 calculated by (Brilliantov et al., 1996; Silbert et al., 2001)

$$20 \quad \vec{F}_{ij}^n = -\frac{4}{3}Y^*\sqrt{R^*}\delta_n^{3/2}\vec{n}_{ij} - 2\sqrt{\frac{5}{6}m^*S_n\beta v_n}\vec{n}_{ij} \quad (19)$$

21
 22 where $Y^* = Y/2/(1 - \nu^2)$ is the equivalent Young's modulus; $\delta_n = 0.5(d_i + d_j) -$
 23 $|\vec{x}_i - \vec{x}_j|$ is the normal overlap; $m^* = m_i m_j / (m_i + m_j)$ is the equivalent particle
 24 mass; $S_n = 2Y^*\sqrt{R^*}\delta_n$ is the normal contact stiffness; $R^* = d_i d_j / 2 / (d_i + d_j)$ is
 25 the equivalent particle radius; β is related to the coefficient of restitution e_n by the
 26 relationship $\beta = \ln e_n / \sqrt{(\ln e_n)^2 + \pi^2}$; and $v_n = \vec{v}_{ij} \cdot \vec{n}_{ij}$. The first term on the right-

1 hand side of Eq. (18) represents the elastic force described by Hertz's theory, and the
 2 second term represents the viscous force reflecting the inelastic collisions between
 3 sand particles. Similarly, the tangential collisional force, which is limited by the
 4 Coulomb friction, is given as (Brilliantov et al., 1996; Silbert et al., 2001)

5

$$6 \quad \vec{F}_{ij}^t = \begin{cases} -8G^* \sqrt{R^* \delta_n} \delta_t \vec{t}_{ij} - 2 \sqrt{\frac{5}{6}} m^* S_t \beta v_t \vec{t}_{ij}, & \text{if } |\vec{F}_{ij}^t| \leq \gamma_s |\vec{F}_{ij}^n| \\ -\gamma_s |\vec{F}_{ij}^n| \vec{t}_{ij}, & \text{if } |\vec{F}_{ij}^t| > \gamma_s |\vec{F}_{ij}^n| \end{cases} \quad (20)$$

7

8 where $G^* = G/2/(2 - \nu)$ is the equivalent shear modulus; δ_t is the tangential
 9 overlap; $\vec{t}_{ij} = \vec{v}_{ij}^t / |\vec{v}_{ij}^t|$ is the tangential unit vector at the contact point; $S_t =$
 10 $8G^* \sqrt{R^* \delta_n}$ is the tangential stiffness; $v_t = \vec{v}_{ij} \cdot \vec{t}_{ij}$; and γ_s is the coefficient of static
 11 friction. The torque on the i -th particle arising from the j -th particle collisional force
 12 is defined as (Haff and Anderson, 1993)

13

$$14 \quad \vec{M}_{ij}^c = 0.5 d_i \vec{n}_{ij} \times \vec{F}_{ij}^t \quad (21)$$

15

16 To account for the significant rolling friction, we apply a rolling resistance torque
 17 (Ai et al., 2011)

18

$$19 \quad \vec{M}_{ij}^r = -\gamma_r R^* |\vec{F}_{ij}^n| \vec{\omega}_{ij} \quad (22)$$

20

21 on each colliding particle, where μ_r is the coefficient of rolling friction, and $\vec{\omega}_{ij} =$
 22 $(\vec{\omega}_{p,i} - \vec{\omega}_{p,j}) / |\vec{\omega}_{p,i} - \vec{\omega}_{p,j}|$ is the unit vector of relative angular velocity.

23

24 3.3 Particle-bed collisions

25 As a saltating particle collides with the sand bed, it has not only a chance to

1 rebound but also may eject several particles from the sand bed. For simplicity, we use
 2 a probabilistic representation, termed as “splash function”, to describe the particle-
 3 bed interactions quantitatively (Kok et al., 2012; Shao, 2008). Currently, the splash
 4 function is primarily characterized by wind-tunnel and numerical simulations (e.g.
 5 Anderson and Haff, 1991; Haff and Anderson, 1993; Huang et al., 2017; Rice et al.,
 6 1996). The rebounding probability of a saltating particle colliding with the sand bed is
 7 approximately by (Anderson and Haff, 1991)

8

$$9 \quad P_{reb} = 0.95[1 - \exp(-v_{imp})] \quad (23)$$

10

11 where v_{imp} is the impact speed of the saltating particle. The kinetic energy of the
 12 rebounding particles is taken as 0.45 ± 0.22 of the impact particle (Kok and Renno,
 13 2009). The rebounding angles θ and φ , as depicted in Fig. 3a, obey an exponential
 14 distribution with a mean value of 40° , i.e. $\theta \sim \text{Exp}(40^\circ)$, and a normal distribution
 15 with parameters $0 \pm 10^\circ$, i.e. $\varphi \sim \text{N}(0^\circ, 10^\circ)$, respectively (Dupont et al., 2013; Kok
 16 and Renno, 2009).

17 It is reasonable to assume that the number of ejected particles depends on the
 18 impact speed and its cross-sectional area. Thus, the number of ejected particles from
 19 the k -th particle bin is (Kok and Renno, 2009)

20

$$21 \quad N_k = \frac{0.02}{\sqrt{gD_{250}}} \frac{D_{imp}}{D_{eje}^k} p_k v_{imp} \quad (24)$$

22

23 where $D_{250} = 0.25 \times 10^{-4}$ m is a reference diameter; D_{imp} and D_{eje}^k are the
 24 diameter of the impact and ejected particles, respectively; and p_k is the mass
 25 fraction of the k -th particle bin. The speed of the ejected particles obeys an
 26 exponential distribution with the mean value taken as $0.6[1 - \exp(-v_{imp}/40/$
 27 $\sqrt{gD_{250}})]$ (Kok and Renno, 2009). Similar to the rebound process, the ejected angles

1 θ and φ are assumed to be $\theta \sim \text{Exp}(50^\circ)$ and $\varphi \sim N(0^\circ, 10^\circ)$.

2

3 **3.4 Particle charge exchanges**

4 In this study, the calculation of the charge transfer between sand particle
5 collisions is based on the asymmetric contact model, assuming that the electrons
6 trapped in high energy states on one particle surface can relax to the other particle
7 surface (Hu et al., 2012; Kok and Lacks, 2009). Thus, the net increment of the charge
8 of particle i after colliding with particle j , Δq_{ij} , can be determined by

9

$$10 \quad \Delta q_{ij} = -e(\rho_h^j S_j - \rho_h^i S_i) \quad (25)$$

11

12 where $e = 1.602 \times 10^{-19}$ C is the elementary charge; ρ_h^i is the density of the
13 electrons trapped in the high energy states on the surface of particle i (assuming that
14 all particles have an identical initial value, i.e., $\rho_h^i = \rho_h^0$), which is modified as

15

$$16 \quad \rho_{h,i}^{\text{after}} = \rho_{h,i}^{\text{before}} - \frac{\Delta q_{ij}}{e\pi d_i^2} \quad (26)$$

17

18 due to collisions between particle i and j ; S_i is the particle contact area, which can
19 be approximately calculated as a line integral along the contact path L_i of particle i

20

$$21 \quad S_i = 2 \int_{L_i} \sqrt{R^* \delta_n} dl_i \quad (27)$$

22

23 where dl_i is the differential of the contact length. In general, when two particles are
24 in contact with each other, the relative sliding motion between the two particles
25 results in two unequal contact areas S_i and S_j , thus producing net charge transfer
26 Δq_{ij} between the two particles. If the particle's net electrical charge is known, its
27 charge-to-mass ratio can be easily determined.

28

3.5 Particle-phase statistics

Similar to particle momentum flux (i.e. Eq. 14), particle horizontal mass flux q , total mass flux Q , mean particle mass concentration m_c (Carneiro et al., 2013; Dupont et al., 2013), and mean particle charge-to-mass ratio $\langle \zeta_p \rangle$ can be numerically determined by

$$q(z) = \frac{\sum m_{p,i} u_{p,i}}{L_x L_y \Delta z} \quad (28a)$$

$$Q = \frac{\sum m_{p,i} u_{p,i}}{L_x L_y} \quad (28b)$$

$$m_c(z) = \frac{\sum m_{p,i}}{L_x L_y \Delta z} \quad (28c)$$

$$\langle \zeta_p \rangle(z) = \frac{\sum \zeta_{p,i} m_{p,i} u_{p,i}}{\sum m_{p,i} u_{p,i}} \quad (28d)$$

where the summation \sum is performed over the saltating particles located in the range of $[z, z + \Delta z]$ for q , m_c , and $\langle \zeta_p \rangle$, but it is performed over all saltating particles for Q . Here, we define the $\langle \zeta_p \rangle$ as the ratio of charge flux and mass flux in the range of $[z, z + \Delta z]$.

3.6 Model implementation

We consider polydisperse soft-spherical sand particles having log-normal mass distribution in a 3-D computational domain $0.5 \text{ m} \times 0.1 \text{ m} \times 1.0 \text{ m}$ (as shown in Fig. 4a), with periodic boundary conditions in the x and y directions. Here, the upper boundary is set to be high enough so that the particle escapes from the upper boundary can be avoided. To reduce the computational cost, the spanwise dimension is chosen as $L_y = 0.1$, since the saltating particles are mainly moving along the streamwise direction.

As shown in Fig. 4b, the model is initiated by randomly releasing 100 uncharged

1 particles, within the region below 0.3 m, and then such released particles begin to
 2 move under the action of the initial log-law wind flow, triggering saltation through a
 3 series of particle-bed collisions. We use cell-based collision searching algorithms,
 4 which perform collision search for particles located in the target cell and its
 5 neighboring cells, to find the midair colliding pairs. The random processes, particle-
 6 bed collisions described previously, are simulated using a general method called the
 7 inverse transformation. The particle motion and wind flow equations are integrated by
 8 predictor-corrector method AB3AM4; that is, 3-order Adams-Bashforth method to
 9 perform prediction and 4-order Adams-Moulton method to perform the correction.
 10 One of the main advantages of using such multi-step integration method is that the
 11 accuracy of results is not sensitive to the detection of exact moments of collision (Tuley
 12 et al., 2010). The charge transfer between the colliding pairs is caused by their
 13 asymmetric contact and can be determined by Eqs. (25)-(27). When calculating
 14 particle-bed charge transfer, the bed is regarded as an infinite plane. According to the
 15 law of charge conservation, the surface charge density of the infinite bed plane and
 16 the newly ejected particles, σ , is (Kok and Renno, 2008; Zhang et al., 2014)

17

$$18 \quad \sigma = - \int_{z_0}^{+\infty} \rho_c(z) dz \quad (29)$$

19

20 where ρ_c is the space charge density. For modelling pure saltation, the E-field is
 21 calculated by Gauss's law (e.g. Zhang et al., 2014). For modelling saltation during dust
 22 storms, the 3-D E-field is directly formulated by Eq. (9) based on our field
 23 measurements, as mentioned above. The variables used in this study are listed and
 24 described in Table 1.

25

26 **4. Results**

27 **4.1. Vertical profiles of 3-D E-field**

28 On May 6, 2014, field measurements began at ~12:00 due to the limited power

1 supply by solar panels. As shown in Fig. 5, although the early stage of dust storm has
 2 not been observed completely, we successfully recorded data of about 8 hours, which
 3 is substantial enough to reveal the pattern of 3-D E-field. From Fig. 5, it can be seen
 4 that, the relative magnitudes of E_1 , E_2 , and E_3 vary with height. For example, the
 5 magnitude of E_3 is larger than that of E_1 and E_2 at 0.15 m height (Fig. 5k) but is
 6 smaller than that of E_1 and E_2 at 0.7 m height (Fig. 5n). The vertical profiles of the
 7 normalized streamwise, spanwise, and vertical components of E-field are shown in Figs.
 8 6a-6c, respectively. To the best of our knowledge, these data are the first measured 3-
 9 D E-field data in the sub-meter layer during dust storms. Numerous studies showed
 10 that the vertical component of E-field in pure saltation decreased with increasing
 11 height (e.g., Kok and Renno, 2008; Schmidt et al., 1998; Zhang et al., 2014).
 12 Interestingly, Fig. 6c shows that during dust storms, all normalized components, E_1^*
 13 to E_3^* , decreases monotonically as height increases in the saltation layer (i.e. $z^* \leq 1$),
 14 similar to the pattern of vertical component in pure saltation.

15 As shown in Figs. 6a-6c, in different periods, each component of the normalized
 16 3-D E-field roughly collapses on a single 3-order polynomial curve (with $R^2=0.67-0.97$,
 17 see Table 2 for details). This suggests that during dust storms, the 3-D E-field in the
 18 sub-meter layer can be characterized as $\langle \overline{E}_i \rangle E_i^*$, where E_i^* represents the pattern of
 19 the dimensionless E-field vertical profile (formulated by Eq. 9), and $\langle \overline{E}_i \rangle$ represents
 20 the height-averaged time-varying mean defined in Eq. (6). It is worth noting that the
 21 E-field pattern E_i^* and their intensities $\langle \overline{E}_i \rangle$ are strongly dependent on the saltation
 22 conditions, such as dust mass loading, temperature, relative humidity (RH), etc. For
 23 example, at given ambient temperature and RH, the mean E-field intensities $\langle \overline{E}_i \rangle$
 24 increases linearly with dust mass loading (e.g. Esposito et al., 2016; Zhang et al., 2017).
 25 In addition, both E_i^* and $\langle \overline{E}_i \rangle$ could vary from event to event, among them, the
 26 saltation conditions are quite different. So far, a quantitative representation of $\langle \overline{E}_i \rangle$ is
 27 challenging due to its high complexity, and thus we regard it as a basic parameter in

1 the following sections for exploring the effects of 3-D E-field on saltation. The fitting
2 results of Eq. (9) are listed in Table 2, with coefficients as rounded to two decimals. The
3 formulations of the 3-D E-field can be readily substituted into the numerical model (i.e.
4 Eq. 11a).

6 **4.2. Effects of particle-particle midair collisions on saltation**

7 Before quantifying the effects of 3-D E-field on saltation by our numerical model,
8 we draw a comparison of several key physical quantities between the simulated results
9 and measurements in the case of pure saltation, in order to ensure the convergence
10 and validity of our numerical code, as shown in Figs. 7a-7c. It is clearly shown that the
11 saltation eventually reaches a dynamic steady-state after ~ 4 seconds. The number of
12 the impacting particles (~ 72 grains) is equal to the sum of the rebounding (~ 50 grains)
13 and the ejected particles (~ 22 grains) during the time interval of 10^{-4} s. At steady-state,
14 each impacting particle, on average, produces a single saltating particle, either by
15 rebound or by ejection. As shown in Fig. 7b, the total mass flux is well predicted by our
16 numerical model, and midair collisions enhance the total mass flux dramatically,
17 especially for less particle viscous dissipation (i.e. large e_n) and large friction velocity.
18 As in previous studies (e.g. Haff and Anderson, 1993; Carneiro et al., 2013), the
19 selected e_n is larger than 0.5 since the e_n of quartz sand particles has been
20 expected to lie in the range of ~ 0.5 - 0.6 (Haff and Anderson, 1993; Kok et al., 2012).
21 Also, the predicted charge-to-mass ratios of saltating particles are widely distributed
22 from -400 to $+60 \mu\text{C kg}^{-1}$, consistent with the previous measurements of charge-to-
23 mass ratio in pure saltation (Bo et al., 2014; Schmidt et al., 1998; Zheng et al., 2003).
24 To our knowledge, so far there are no actual measurements of charge on a single sand
25 particle in dust events. In the case of Fig. 7c, the magnitude of the simulated mean
26 charge-to-mass ratio is around $100 \mu\text{C kg}^{-1}$, corresponding to a mean charge of
27 1.64×10^{-12} C/particle. This is in accordance with the empirical values of 10^{-14} - 10^{-12}
28 C/particle (Merrison, 2012).

29 In addition to affecting sand transport, midair collisions also affect charge

1 exchanges between saltating particles. When considering midair collisions, the charge-
2 to-mass ratio distribution shifts slightly toward zero as the wind velocity increases, as
3 shown in Figs. 8a-8c. As wind speed increases, the difference of the charge-to-mass
4 ratio distribution between the cases with and without midair collisions is increasingly
5 notable. This is because the probability of midair collisions become more significant
6 for larger wind speed (Sørensen and McEwan, 1996; Huang et al., 2007).

8 **4.3. Effects of 3-D E-field on saltation**

9 By substituting the formulations of the 3-D E-field (i.e. $\langle \overline{E}_i \rangle E_i^*$, $i = 1,2,3$) into our
10 model (i.e. Eq. 11a), we then evaluate the effects of 3-D E-field on saltation during
11 storms properly. As shown in Fig. 9a, compared to the case without E-field, the vertical
12 component of the E-field (i.e. 1-D E-field) inhibits mass flux, in agreement with
13 previous studies (Kok and Renno, 2008; Zheng et al., 2003). However, the mass flux is
14 enhanced by 3-D E-field, causing the simulated value closer to our measured data.
15 Such enhancement of mass flux by 3-D E-field can be qualitatively explained by the
16 considerable enhancements of m_c below ~ 0.02 m height (Fig. 10a) and $\langle u_p \rangle$ in the
17 range from 0.01 to 0.1 m height (Fig. 10b), due to the streamwise and spanwise
18 components. Meanwhile, although the saltation height is not sensitive to E-field
19 vertical component, 3-D E-field enhances the saltation height significantly and,
20 therefore, makes the numerical prediction more accurate (Fig. 9b). This is because
21 when considering the E-field vertical component, the mass flux profile is very similar
22 to the case of no E-field consideration (Figs. 9a and 10). In contrast, 3-D E-field distorts
23 the mass flux profile (as well as m_c and $\langle u_p \rangle$), and thus alters saltation height
24 significantly (Figs. 9a and 10).

25 Additionally, we also explore how the key parameter, the density of charged
26 species ρ_h^0 , affects saltation, as shown in Figs. 11a-11c. Since the height-averaged
27 time-varying mean is strongly dependent on the ambient conditions such as
28 temperature and RH, the height-averaged time-varying mean is set at two different
29 levels. The predicted results show that, at each height-averaged time-varying mean

1 level, the magnitude of the mean charge-to-mass ratio increases with increasing ρ_h^0 ,
2 and then reaches a relative equilibrium value at approximately $\rho_h^0 = 10^{18} \text{ m}^{-2}$ (Fig.
3 10a), thus leading to the constant enhancement of total mass flux Q and saltation
4 height z_{salt} (Figs. 10b and 10c). From Eqs. (25)-(26), it can be seen that the net charge
5 transfer Δq_{ij} is proportional to the initial density ρ_h^0 so that $\langle \zeta_p \rangle$ increases rapidly
6 with increasing ρ_h^0 for small ρ_h^0 . However, for larger ρ_h^0 , Δq_{ij} is no longer
7 proportional to ρ_h^0 because in this case the difference of the number of trapped
8 electrons between two colliding particles (i.e. $\rho_h^j S_j - \rho_h^i S_i$) has the same value and
9 ρ_h^0 is not the key parameter for determining the mean charge-to-mass ratio (Kok and
10 Lacks, 2009). Fig. 11c shows a peak of increase in z_{salt} at ρ_h^0 of about 10^{16} - 10^{17} m^{-2} ,
11 because $\langle \zeta_p \rangle$ also exhibits a peak in the same range of ρ_h^0 . In addition, the peak is
12 more apparent in Fig. 11c. This is because z_{salt} is very sensitive to the mass flux
13 profile. A little change in mass flux profile can lead to an apparent change in z_{salt} (see
14 Text S1 in the Supplement). For the larger height-averaged time-varying mean, the
15 enhancements of the total mass flux Q and saltation height z_{salt} could exceed 20 %
16 and 15 %, respectively.

17

18 **5. Discussion**

19 **5.1. Field measurements of 3-D E-field in the sub-meter layer**

20 To determine the effects of particle triboelectric charging on saltation precisely,
21 3-D E-field measurements in the saltation layer (i.e. sub-meter above the ground) is
22 required. Although the E-field measurements, such as Bo and Zheng (2013), Esposito
23 et al. (2016), Kamra (1972), Rudge (1913), Williams et al. (2009), and Zhang et al. (2017)
24 in dust storms are numerous, 3-D E-field in the sub-meter layer has not been studied
25 so far. This is because the traditional atmospheric E-field sensors, such as CS110 sensor
26 manufactured by Campbell Scientific, Inc., have dimensions of $15.2 \times 15.2 \times 43.2 \text{ cm}^3$
27 (e.g. Esposito et al., 2016; Yair et al., 2016), which is too large compared to the height
28 of saltation layer. Thus, it will lead to significant disturbances in the ambient E-field.
29 Fortunately, the diameter of the VREFM sensor developed by Lanzhou University is

1 only 2.5 cm and thus could considerably eliminate the E-field disturbances (Zhang et
2 al., 2017; Zheng, 2013). In this study, using the VREFM sensors, we have measured and
3 characterized the 3-D E-field from 0.05 to 0.7 m height during dust storms, which can
4 provide valuable data for investigating the mechanisms of particle triboelectric
5 charging in saltation.

6 In E-field data analysis, the E-field is normalized by its time-varying mean over a
7 certain timescale, which can be extracted by the DWT and EEMD methods with
8 negligible end effects and mode mixing (Percival and Walden, 2000; Wu and Huang,
9 2009). At the same time, since the saltation height z_{salt} slightly varies with time (i.e.
10 0.172 ± 0.0343 m, see Fig. S3 in the supplement), the height z above the ground is
11 normalized by the mean saltation height \bar{z}_{salt} . Note that we calculate the saltation
12 height and mass flux over every 30-min time interval because the sufficiently long
13 period is needed to capture all scales of turbulence (Martin and Kok, 2017; Sherman
14 and Li, 2012). The 3-D E-field pattern is finally characterized as the 3-order polynomials,
15 but it is only valid in the range that is not too far beyond the measurement points.
16 Additionally, the 3-D E-field pattern of dust storms may vary event to event, because
17 it is strongly related to the driving mechanisms of dust storms, such as monsoon winds,
18 squall lines, and thunderstorms (Shao, 2008), and ambient conditions, such as
19 temperature and relative humidity (Esposito et al., 2016; Zhang and Zheng, 2018).
20 Although the 3-D E-field pattern revealed in this study may not be a universal feature,
21 the proposed E-field data analysis method can be easily applied to other cases.

22

23 **5.2. Potential mechanisms for generating intense horizontal E-field in dust storms**

24 Like many previous studies, the E-field can be simplified to 1-D (i.e. vertical
25 component) in pure saltation (e.g. Kok and Renno, 2008), since in such cases the
26 magnitude of the streamwise and spanwise components is much less than that of
27 vertical component (Zhang et al., 2014). However, during dust storms, the streamwise
28 and spanwise components of the E-field are consistently larger than the vertical
29 component, as mentioned previously. E-field is therefore 3-D in dust storms. In

1 contrast to the vertical component which is closely related to the total mass loading
2 (Esposito et al., 2016; Williams et al., 2009), the intense streamwise and spanwise
3 components of the E-field in dust storms may be aerodynamically created by the
4 unsteady wind flows (Zhang et al., 2014) and turbulent fluctuations (Cimarelli et al.,
5 2013; Renzo and Urzay, 2018). It is well-known that dust storm is a polydisperse (having
6 dust particles with diameters from $<10\ \mu\text{m}$ to $\sim 500\ \mu\text{m}$) particle-laden turbulent flow
7 at very high-Reynolds-number (up to $\sim 10^8$). The wind flow in dust storms is certainly
8 unsteady and random. Numerical simulation by Zhang et al. (2014) showed that the
9 unsteady incoming flow could lead to the nonuniform transport of charged particles
10 in the streamwise direction and thus resulted in fluctuating streamwise and vertical E-
11 fields. In addition to unsteadiness, recent direct numerical simulation (Renzo and Urzay,
12 2018) and laboratory experiment (Cimarelli et al., 2013) of particle-laden turbulent
13 flows demonstrated that the generation of 3-D E-field could be caused by turbulent
14 fluctuations. That is, the negatively charged small particles are affected by local
15 turbulence and tend to accumulate in the interstitial regions between vortices, while
16 the positively charged larger particles are unresponsive to turbulent fluctuations and
17 are more uniformly distributed than the smaller (Cimarelli et al., 2013; Renzo and Urzay,
18 2018). We thus reasonably expect that the negatively charged finer dust particles (<10
19 μm) accumulate in specific regions, while the positively charged coarser sand particles
20 ($>100\ \mu\text{m}$) are more uniformly distributed due to its large inertia. Doubtless, such
21 charge segregation could produce 3-D E-field (e.g. Renzo and Urzay, 2018). To sum up,
22 the generating mechanisms responsible for the streamwise and spanwise E-fields in
23 dust storms are probably the charge segregation caused by unsteady wind flows and
24 turbulent fluctuations.

25 Additionally, one possible explanation for the intense streamwise and spanwise
26 E-fields is that there exist large- and very-large-scale motions in atmospheric surface
27 flows, leading to a large extent charge segregation in the streamwise and spanwise
28 directions. In atmospheric surface layer flows, the largest vortices or coherent motions
29 of the wind flows are found to be compared to the boundary layer thickness (~ 60 - 200

1 m) (Kunkel and Marusic, 2006; Hutchins et al., 2012). This may lead to a phenomenon
2 that the charged particles are more nonuniformly distributed (over a larger spatial
3 scale) in the streamwise and spanwise directions than in the vertical direction.
4 Accordingly, the intensity of the streamwise and spanwise E-fields is probably larger
5 than that of the vertical E-field.

6 7 **5.3. Particle-particle triboelectric charging resolved model**

8 Although most physical mechanisms, such as asymmetric contact, polarization by
9 external E-fields, statistical variations of material properties and shift of aqueous ions,
10 are responsible for particle triboelectric charging, contact or triboelectric charging is
11 the primary mechanism (e.g. Harrison et al., 2016; Lacks and Sankaran, 2011; Zheng,
12 2013). In the previous model, however, the charge-to-mass ratios of the saltating
13 particles are either assumed to be a constant value (e.g. Schmidt et al., 1998; Zhang et
14 al., 2014; Zheng et al., 2003) or are not accounted for in the particle-particle midair
15 collisions (e.g. Kok and Renno, 2008). In this study, by using DEM together with an
16 asymmetric contact electrification model, we account for the particle-particle
17 triboelectric charging during midair collisions in saltation. The DEM implemented by
18 cell-based algorithms is effective to detect and evaluate most of the particle-particle
19 midair collisional dynamics (Norouzi et al., 2016). Meanwhile, the charge transfer
20 between colliding particles can be determined by Eqs. (25) and (26). Compared to the
21 previous studies (e.g. Kok and Lacks, 2009), the main innovation of this model is that
22 the comprehensive consideration of the particle collisional dynamics affecting particle
23 charge transfer is involved. In summary, the present model is a particle-particle midair
24 collision resolved model, and the predicted charge-to-mass ratio agrees well with the
25 published measurement data (see Fig. 7c). These findings indicate that midair
26 collisions in saltation are important, both in momentum and charge exchanges.

27 One limitation of our model is that the effects of turbulent fluctuations on particle
28 charging and dynamics are not explicitly accounted for. In actual conditions, saltation
29 is unsteady and inhomogeneous at small scales, and the wind flow is mathematically

1 described by the continuity and Navier-Stokes equations. However, in many cases,
2 wind flow is statistically steady and homogeneous over a typical timescale of 10 min
3 (Durán et al., 2011; Kok et al., 2012). For example, in the relatively stationary period in
4 Fig.5, all long-period averaged statistics become independent of time. In this case, the
5 governing equations of the wind flow can be reduced to a simple model described by
6 equation Eq. (13). There is no doubt that 3-D turbulent fluctuations could affect
7 particle charging and dynamics considerably (e.g. Cimorelli et al., 2013; Dupont et al.,
8 2013). Further work is therefore needed to incorporate turbulence into the numerical
9 model.

11 **5.4. Implications for evaluating particle triboelectric charging in dust events**

12 It is generally accepted that E-field could considerably affect the lifting and
13 transport of sand particles. As the findings of previous 1-D E-field models (e.g. Kok and
14 Renno, 2008), the E-field has been proven to inhibit sand transport in our model, when
15 considering the vertical component of the E-field alone. It is worth noting that, unlike
16 the natural 1-D E-field produced by the charged sand particles, the man-made 1-D E-
17 field may enhance sand transport in pure saltation. For example, Rasmussen et al.
18 (2009) found that sand mass flux in pure saltation is significantly enhanced when a
19 downward-pointing external E-field (opposite to the direction of actual vertical E-field)
20 with a magnitude of 270 kV m^{-1} is applied. In contrast to the 1-D E-field, our model
21 further shows that the real 3-D E-field in dust storms enhances sand transport
22 substantially, consistent with a recent measurement by Esposito et al. (2016). This 3-D
23 E-field model may resolve the discrepancy between the 1-D E-field model in pure
24 saltation (e.g. Kok and Renno, 2008) and the recent measurement in dust storms (i.e.
25 Esposito et al., 2016). In addition, the saltation height has also been enhanced by 3-D
26 E-field. Therefore, it is necessary to consider 3-D E-field in further studies.

27 However, a remaining critical challenge is still to simulate particle triboelectric
28 charging in dust storms precisely. The driving atmospheric turbulent flows having a
29 typical Reynolds number on the order of 10^8 cover a broad range of length and time

1 scales, which needs huge computational cost to resolve (e.g. Shao, 2008). On the other
2 hand, particle triboelectric charging is so sensitive to particle's collisional dynamics
3 that it needs to resolve each particle collisional dynamics (e.g. Hu et al., 2012; Lacks
4 and Sankaran, 2011). To model the particle's collisional dynamics properly, the time
5 steps of DEM are generally from 10^{-7} to 10^{-4} s (Norouzi et al., 2016). However, steady-
6 state saltation motion often requires several seconds to several tens of seconds to
7 reach the equilibrium state. In this study, when $u_* = 0.5 \text{ m s}^{-1}$ and the computational
8 domain is $0.5 \times 0.1 \times 1.0 \text{ m}^3$, the total number of saltating particles exceeds 7×10^4 (Fig.
9 S8 in the Supplement). Consequently, the triboelectric charging in saltation is currently
10 very difficult to simulate, where a large number of polydisperse sand particles, the high
11 Reynolds-number turbulent flow, and the inter-particle electrostatic forces are
12 mutually coupled. In the present version of the model, we do not consider the particle-
13 particle interactions such as particle agglomeration and fragmentation during particle
14 collision or frictional contact, as well as the particle-turbulence interaction that is the
15 effects of turbulent fluctuations on the triboelectric charging and dynamics of particles.
16 Further studies require considerable effort to incorporate these interactions into a
17 tractable numerical model, especially turbulence, which is very important for large
18 wind velocity.

20 **6. Conclusions**

21 Severe dust storms occurring in arid and semiarid regions threaten human lives
22 and result in substantial economic damages. Intense E-field up to $\sim 100 \text{ kV m}^{-1}$ does
23 exist in dust storms and could strongly affect particle dynamics. In this study, we
24 performed the field measurements of 3-D E-field in the sub-meter layer from 0.05 to
25 0.7 m above the ground during dust storms by VREFM sensors. Meanwhile, by
26 introducing the DEM and asymmetric charging mechanism into the saltation model,
27 we numerically study the effects of 3-D E-field on saltation. Overall, our results show
28 that: (1) measured 3-D E-field data roughly collapse on the 3-order polynomial curves
29 when normalized, providing a simple representation of the 3-D E-field during dust

1 storms for the first time; (2) the inclusion of 3-D E-field in saltation model may resolve
2 the discrepancy between previous 1-D E-field model (e.g. Kok and Renno, 2008) and
3 measurements (Esposito et al., 2016) in the aspect of whether the E-field inhibits or
4 enhances saltation; (3) midair collisions dramatically affect both momentum and
5 charge exchanges between saltating particles; and (4) the model predicts that 3-D E-
6 field enhances the total mass flux and saltation height significantly, suggesting that 3-
7 D E-field should be considered in future models, especially for dust storms.

8 We have also performed discussions about various sensitive parameters such as
9 the density of charged species, the coefficient of restitution, and the height-averaged
10 time-varying mean of the 3-D E-field. These results significantly add new knowledge to
11 the role of particle triboelectric charging in determining the transport and lifting of
12 sand and dust particles. A great effort is further needed to understanding the
13 interactions such as particle agglomeration and fragmentation, as well as the effects
14 of the turbulence on the triboelectric charging and dynamics of particles.

15

16 **Data availability**

17 The E-field data recorded in our field campaign are provided as a CSV file in the
18 Supplement.

19

20 **Author contribution**

21 H.Z. performed the field observations, numerical simulation, and data analyses as
22 well as wrote the manuscript, which was guided and edited by Y.H.Z. All authors
23 discussed the results and commented on the manuscript.

24

25 **Competing interests**

26 The authors declare that they have no conflict of interest.

27

28 **Acknowledgments**

29 We thank the editor and anonymous reviewers for their insightful comments that

1 greatly improve the final manuscript. This work was supported by the National Natural
2 Science Foundation of China (grant number 11802109), the Young Elite Scientists
3 Sponsorship Program by CAST (grant number 2017QNRC001), and the Fundamental
4 Research Funds for the Central Universities (grant number lzujbky-2018-7).

5

6 **References**

7 Ai, J., Chen, J. F., Rotter, J. M., and Ooi, J. Y.: Assessment of rolling resistance models in
8 discrete element simulations, *Powder Technol.*, 206, 269–282,
9 doi:10.1016/j.powtec.2010.09.030, 2011.

10 Anderson, R. S., and Hallet, B.: Sediment transport by wind: toward a general model,
11 *Geol. Soc. Am. Bull.*, 97, 523–535, doi: 10.1130/0016-
12 7606(1986)97<523:STBWTA>2.0.CO;2, 1986.

13 Anderson, R. S., and Haff, P. K.: Simulation of eolian saltation, *Science*, 241, 820–823,
14 doi:10.1126/science.241.4867.820, 1988.

15 Anderson, R. S., and Haff, P. K.: Wind modification and bed response during saltation
16 of sand in air, *Acta Mech.*, 1, 21–51, doi:10.1007/978-3-7091-6706-9_2, 1991.

17 Bagnold, R.: *The Physics of Blown Sand and Desert Dunes*, Chapman & Hall, London,
18 1941.

19 Bendat, J. S., and Piersol, A. G.: *Random data: analysis and measurement procedures*,
20 John Wiley & Sons, Hoboken, 2011.

21 Bo, T. L., Zhang, H., and Zheng, X. J.: Charge-to-mass ratio of saltating particles in wind-
22 blown sand, *Sci. Rep.*, 4, 5590, doi:10.1038/srep05590, 2014.

23 Bo, T. L., and Zheng, X. J.: A field observational study of electrification with in a dust
24 storm in Minqin, China, *Aeolian Res.*, 8, 39–47, doi:10.1016/j.aeolia.2012.11.001,
25 2013.

26 Brilliantov, N. V., Spahn, F., Hertzsch, J. M., and Poschel, T.: Model for collisions in
27 granular gases, *Phys. Rev. E*, 53, 5382, doi:10.1103/PhysRevE.53.5382, 1996.

28 Carneiro, M. V., Araújo, N. A., Pähtz, T., and Herrmann, H. J.: Midair collisions enhance
29 saltation, *Phys. Rev. Lett.*, 115, 058001, doi:10.1103/PhysRevLett.111.058001,

1 2013.

2 Cheng, N. S.: Simplified settling velocity formula for sediment particle, *J. Hydraul. Eng.*,

3 123, 149–152, doi:10.1061/(ASCE)0733-9429(1997)123:2(149), 1997.

4 Cimarelli, C., Alatorre-Ibargüengoitia, M. A., Kueppers, U., Scheu, B., and Dingwell, D.

5 B.: Experimental generation of volcanic lightning, *Geology*, 42, 79–82, doi:

6 10.1130/G34802.1, 2014.

7 Daubechies, I. (1990). The wavelet transform, time-frequency localization and signal

8 analysis. *IEEE transactions on information theory*, 36(5), 961–1005.

9 Dupont, S., Bergametti, G., Marticorena, B., and Simoens, S.: Modeling saltation

10 intermittency, *J. Geophys. Res.-Atmos.*, 118, 7109–7128, doi:10.1002/jgrd.50528,

11 2013.

12 Durán, O., Claudin, P., and Andreotti, B.: On aeolian transport: Grain-scale interactions,

13 dynamical mechanisms and scaling laws, *Aeolian Res.*, 3, 243 – 270, doi:

14 10.1016/j.aeolia.2011.07.006, 2011.

15 Esposito, F., Molinaro, R., Popa, C.I., Molfese, C., Cozzolino, F., Marty, L., Taj-Eddine, K.,

16 Achille, G. D., Franzese, G., and Silvestro, S.: The role of the atmospheric electric

17 field in the dust lifting process, *Geophys. Res. Lett.*, 43, 5501–5508,

18 doi:10.1002/2016GL068463, 2016.

19 Flandrin, P., Rilling, G., and Goncalves, P.: Empirical mode decomposition as a filter

20 bank, *IEEE Signal Process. Lett.*, 11, 112–114, doi: 10.1109/LSP.2003.821662,

21 2004.

22 Grinsted, A., Moore, J. C., and Jevrejeva, S.: Application of the cross wavelet transform

23 and wavelet coherence to geophysical time series, *Nonlinear Proc. Geoph.*, 11,

24 561–566, doi: 10.5194/npg-11-561-2004, 2004.

25 Haff, P. K., and Anderson, R. S.: Grainscale simulations of loose sedimentary beds: the

26 example of grain-bed impacts in aeolian saltation, *Sedimentology*, 40, 175–198,

27 doi:10.1111/j.1365-3091.1993.tb01760.x, 1993.

28 Harrison, R. G., Barth, E., Esposito, F., Merrison, J., Montmessin, F., Aplin, K. L., Borlina,

1 C., Berthelier, J. J., Dprez, G., and Farrell, W. M.: Applications of electrified dust
2 and dust devil electrodynamics to martian atmospheric electricity, *Space Sci. Rev.*,
3 203, 299–345, doi:10.1007/s11214-016-0241-8, 2016.

4 Hu, W., Xie, L., and Zheng, X.: Contact charging of silica glass particles in a single
5 collision, *Appl. Phys. Lett.*, 101, 114107, doi:10.1063/1.4752458, 2012.

6 Huang, H. J., Bo, T. L., and Zhang, R.: Exploration of splash function and lateral velocity
7 based on three-dimensional mixed-size grain/bed collision. *Granul. Matter*, 19(4),
8 73, doi: 10.1007/s10035-017-0759-9, 2017.

9 Huang, N., Zhang, Y., and D'Adamo, R.: A model of the trajectories and midair collision
10 probabilities of sand particles in a steady state saltation cloud, *J. Geophys. Res.-*
11 *Atmos.*, 112, doi: 10.1029/2006JD007480, 2007.

12 Huang, N. E., Shen, Z., Long, S. R., Wu, M. C., Shih, H. H., Zheng, Q., Yen, N. C., Tung, C.
13 C., and Liu, H. H.: The empirical mode decomposition and the Hilbert spectrum
14 for nonlinear and non-stationary time series analysis, *Proc. R. Soc. A-Math. Phys.*
15 *Eng. Sci.*, 454, 903–995, doi:10.1098/rspa.1998.0193, 1998.

16 Huang, N. E., and Wu, Z.: A review on Hilbert-Huang transform: Method and its
17 applications to geophysical studies, *Rev. Geophys.*, 46, RG2006,
18 doi:10.1029/2007RG000228, 2008.

19 Hutchins, N., Chauhan, K., Marusic, I., Monty, J., and Klewicki, J.: Towards reconciling
20 the large-scale structure of turbulent boundary layers in the atmosphere and
21 laboratory, *Boundary-Layer Meteorol.*, 145, 273–306, doi: 10.1007/s10546-012-
22 9735-4, 2012.

23 Jackson, T. L., and Farrell, W. M.: Electrostatic fields in dust devils: an analog to Mars,
24 *IEEE Trans. Geosci. Remote Sensing*, 44, 2942–2949,
25 doi:10.1109/TGRS.2006.875785, 2006.

26 Kamra, A. K.: Measurements of the electrical properties of dust storms, *J. Geophys.*
27 *Res.*, 77, 5856–5869, doi:10.1029/JC077i030p05856, 1972.

28 Kawamura, R.: Study on sand movement by wind, Technical Report, Institute of Science
29 and Technology, University of Tokyo, 5, 95–112, 1951.

- 1 Kunkel, G. J., and Marusic, I.: Study of the near-wall-turbulent region of the high-
2 Reynolds-number boundary layer using an atmospheric flow, *J. Fluid Mech.*, 548,
3 375–402, doi: 10.1017/S0022112005007780, 2006.
- 4 Kok, J. F., and Lacks, D. J.: Electrification of granular systems of identical insulators, *Phys.*
5 *Rev. E*, 79, 051304, doi:10.1103/PhysRevE.79.051304, 2009.
- 6 Kok, J. F., Parteli, E. J., Michaels, T. I., and Karam, D. B.: The physics of wind-blown sand
7 and dust, *Rep. Prog. Phys.*, 75, 106901, doi:10.1088/0034-4885/75/10/106901,
8 2012.
- 9 Kok, J. F., and Renno, N. O.: Electrostatics in wind-blown sand, *Phys. Rev. Lett.*, 100,
10 014501, doi:10.1103/PhysRevLett.100.014501, 2008.
- 11 Kok, J. F., and Renno, N. O.: A comprehensive numerical model of steady state saltation
12 (COMSALT), *J. Geophys. Res.-Atmos.*, 114, doi:10.1029/2009JD011702, 2009.
- 13 Lacks, D. J., and Sankaran, R. M.: Contact electrification of insulating materials, *J. Phys.*
14 *D-Appl. Phys.*, 44, 453001, doi:10.1088/0022-3727/44/45/453001, 2011.
- 15 Lettau, K., and Lettau, H. H.: Experimental and micro-meteorological field studies of
16 dune migration, in Lettau, K., and Lettau, H. H., eds., *Exploring the World's Driest*
17 *Climate*, Institute for Environmental Studies, University of Wisconsin Madison,
18 110–147, 1978.
- 19 Loth, E.: Lift of a spherical particle subject to vorticity and/or spin, *AIAA J.*, 46, 801–
20 809, doi:10.2514/1.29159, 2008.
- 21 Marticorena, B., and Bergametti, G.: Modeling the atmospheric dust cycle: 1. design
22 of a soil-derived dust emission scheme, *J. Geophys. Res.-Atmos.*, 100, 16415–
23 16430, doi:10.1029/95JD00690, 1995.
- 24 Martin, R. L., and Kok, J. F.: Wind-invariant saltation heights imply linear scaling of
25 aeolian saltation flux with shear stress, *Sci. Adv.*, 3, e1602569, doi:
26 10.1126/sciadv.1602569, 2017.
- 27 Merrison, J. P.: Sand transport, erosion and granular electrification, *Aeolian Res.*, 4, 1–
28 16, doi: 10.1016/j.aeolia.2011.12.003, 2012.
- 29 Minier, J. P.: Statistical descriptions of polydisperse turbulent two-phase flows, *Phys.*

- 1 Rep., 665, 1–122, doi:10.1016/j.physrep.2016.10.007, 2016.
- 2 Norouzi, H. R., Zarghami, R., Sotudeh-Gharebagh, R., and Mostoufi, N.: Coupled CFD-
3 DEM modeling: formulation, implementation and application to multiphase flows,
4 John Wiley & Sons, Chichester, 2016.
- 5 Owen, P. R.: Saltation of uniform grains in air, *J. Fluid Mech.*, 20, 225–242,
6 doi:10.1017/S0022112064001173, 1964.
- 7 Pähtz, T., Omeradžić, A., Carneiro, M. V., Araújo, N. A., and Herrmann, H. J.: Discrete
8 Element Method simulations of the saturation of aeolian sand transport, *Geophys.*
9 *Res. Lett.*, 42, 2063–2070, doi:10.1002/2014GL062945, 2015.
- 10 Percival, D. B., Walden, A. T.: *Wavelet methods for time series analysis*, Cambridge, UK,
11 Cambridge UP, 2000.
- 12 Rasmussen, K. R., Kok, J. F., and Merrison, J. P.: Enhancement in wind-driven sand
13 transport by electric fields, *Planet Space Sci.*, 57, 804–808,
14 doi:10.1016/j.pss.2009.03.001, 2009.
- 15 Di Renzo, M., and Urzay, J.: Aerodynamic generation of electric fields in turbulence
16 laden with charged inertial particles, *Nat. Commun.*, 9, 1 – 11, doi:
17 10.1038/s41467-018-03958-7, 2018.
- 18 Rice, M. A., Willetts, B. B., and McEwan, I. K.: Observations of collisions of saltating
19 grains with a granular bed from high-speed cine-film, *Sedimentology*, 43, 21-31,
20 doi:10.1111/j.1365-3091.1996.tb01456.x, 1996.
- 21 Rudge, W. A. D.: Atmospheric electrification during South African dust storms, *Nature*,
22 91, 31–32, doi:10.1038/091031a0, 1913.
- 23 Schmidt, D. S., Schmidt, R. A., and Dent, J. D.: Electrostatic force on saltating sand, *J.*
24 *Geophys. Res.-Atmos.*, 103, 8997–9001, doi:10.1029/98JD00278, 1998.
- 25 Shao, Y. P.: *Physics and Modelling of Wind Erosion*, Springer Science & Business Media,
26 Heidelberg, 2008.
- 27 Sherman, D. J., and Li, B.: Predicting aeolian sand transport rates: A reevaluation of
28 models, *Aeolian Res.*, 3, 371–378, doi: 10.1016/j.aeolia.2011.06.002, 2012.
- 29 Silbert, L. E., Ertaş, D., Grest, G. S., Halsey, T. C., Levine, D., and Plimpton, S. J.: Granular

1 flow down an inclined plane: Bagnold scaling and rheology, *Phys. Rev. E*, 64,
2 051302, doi:10.1103/PhysRevE.64.051302, 2001.

3 Sørensen, M.: On the rate of aeolian transport, *Geomorphology*, 59, 53–62,
4 doi:10.1016/j.geomorph.2003.09.005, 2004.

5 Sørensen, M., and McEwan, I.: On the effect of mid-air collisions on aeolian saltation,
6 *Sedimentology*, 43, 65–76, doi: 10.1111/j.1365-3091.1996.tb01460.x, 1996.

7 Su, Y., Huang, G., and Xu, Y. L.: Derivation of time-varying mean for non-stationary
8 downburst winds, *J. Wind Eng. Ind. Aerod.*, 141, 39 – 48, doi:
9 10.1016/j.jweia.2015.02.008, 2015.

10 Tuley, R., Danby, M., Shrimpton, J., and Palmer, M.: On the optimal numerical time
11 integration for lagrangian dem within implicit flow solvers, *Comput. Chem. Eng.*,
12 34, 886–899, doi:10.1016/j.compchemeng.2009.10.003, 2010.

13 White, B. R., and Schulz, J. C.: Magnus effect in saltation, *J. Fluid Mech.*, 81, 497–512,
14 doi:10.1017/S0022112077002183, 1977.

15 Williams, E., Nathou, N., Hicks, E., Pontikis, C., Russell, B., Miller, M., and Bartholomew,
16 M. J.: The electrification of dust-lofting gust fronts (haboobs) in the sahel, *Atmos.*
17 *Res.*, 91, 292–298, doi:10.1016/j.atmosres.2008.05.017, 2009.

18 Wu, Z., and Huang, N. E.: Ensemble empirical mode decomposition: a noise-assisted
19 data analysis method, *Adv. Adaptive Data Anal.*, 1, 1–41, doi:
20 10.1142/S1793536909000047, 2009.

21 Wu, Z., Huang, N. E., Wallace, J. M., Smoliak, B. V., and Chen, X.: On the time-varying
22 trend in global-mean surface temperature, *Clim. Dyn.*, 37, 759–773,
23 doi:10.1007/s00382-011-1128-8, 2011.

24 Xie, L., Ling, Y., and Zheng, X.: Laboratory measurement of saltating sand particles’
25 angular velocities and simulation of its effect on saltation trajectory, *J. Geophys.*
26 *Res.-Atmos.*, 112, D12116, doi:10.1029/2006JD008254, 2007.

27 Yair, Y., Katz, S., Yaniv, R., Ziv, B., and Price, C.: An electrified dust storm over the Negev
28 desert, Israel, *Atmos. Res.*, 181, 63–71, doi:10.1016/j.atmosres.2016.06.011,
29 2016.

- 1 Zhang, H., Bo, T. L., and Zheng, X.: Evaluation of the electrical properties of dust storms
2 by multi-parameter observations and theoretical calculations, *Earth Planet. Sci.*
3 *Lett.*, 461, 141–150, doi:10.1016/j.epsl.2017.01.001, 2017.
- 4 Zhang, H., and Zheng, X.: Quantifying the large-scale electrification equilibrium effects
5 in dust storms using field observations at Qingtu Lake Observatory, *Atmos. Chem.*
6 *Phys.*, 18, 17087–17097, doi:10.5194/acp-18-17087-2018, 2018.
- 7 Zhang, H., Zheng, X. J., and Bo, T. L.: Electrification of saltating particles in wind-blown
8 sand: Experiment and theory, *J. Geophys. Res.-Atmos.*, 118, 12086 – 12093.
9 doi:10.1002/532 2013JD020239, 2013.
- 10 Zhang, H., Zheng, X. J., and Bo, T. L.: Electric fields in unsteady wind-blown sand, *Eur.*
11 *Phys. J. E*, 37, 13, doi:10.1140/epje/i2014-14013-6, 2014.
- 12 Zheng, X. J.: Electrification of wind-blown sand: recent advances and key issues, *Eur.*
13 *Phys. J. E*, 36, 138, doi:10.1140/epje/i2013-13138-4, 2013.
- 14 Zheng, X. J., Huang, N., and Zhou, Y. H.: Laboratory measurement of electrification of
15 wind-blown sands and simulation of its effect on sand saltation movement, *J.*
16 *Geophys. Res.-Atmos.*, 108, doi:10.1029/2002JD002572, 2003.
- 17

1 **Table 1.** Description of all variables used in this study.

Symbols	Physical meaning	Units
$a_{0,i}, a_{1,i}, a_{2,i}, a_{3,i}$	fitting coefficients in Eq. (8)	1
C_d	drag coefficient	1
C_m	normalized spin lift coefficient in Magnus force formula	1
d_p	particle diameter	m
d_i, d_j	diameters of particle i and j	m
d_m	mean diameter of particle sample in the numerical model	m
D_{imp}, D_{ej}^k	diameter of the impact and ejected particles	m
e_n	coefficient of restitution of particles	1
E	a time series of measured E-field	kV m ⁻¹
\overline{E}	time-varying mean values of $E(t)$	kV m ⁻¹
$\langle \overline{E}_i \rangle$	height-averaged time-varying mean values of $E(t)$	kV m ⁻¹
$E_i^*(z^*)$	dimensionless E-field of component i	1
E_1, E_2, E_3	streamwise, spanwise, and vertical components of E-field	kV m ⁻¹
\vec{F}_i^d, \vec{F}_i^m	drag force and Magnus force acting on particle i	N
$\vec{F}_{ij}^d, \vec{F}_{ij}^t$	the normal and tangential collisional forces	N
$g=9.81$	gravitational acceleration	m s ⁻²
G	shear modulus of particles	Pa
G^*	equivalent shear modulus between two contacting particles	Pa
I_i	moment of inertia of particle i	kg m ²
L_x, L_y	streamwise and spanwise width of the computational domain	m
m^*	equivalent particle mass between two contacting particles	kg
$m_{p,i}$	mass of particle i	kg
m_c	mean particle mass concentration	kg m ⁻³
$\vec{M}_i^{w-p}, \vec{M}_{ij}^c, \vec{M}_{ij}^r$	torque due to the wind, the torque due to the tangential component of the particle collisional forces, and the rolling resistance torque	N·m
\vec{n}_{ij}	unit vector in the direction from the center of particle i point toward the center of particle j	-
N	number of the decomposition levels of DWT and EEMD	1
N_e	number of white noise series added to the original E-field series	1
N_k	number of ejected particles from the k -th particle bin	1
p_k	mass fraction of the k -th particle bin	1
P_{reb}	rebouncing probability of a saltating particle colliding with the sand bed	1
q, Q	mass flux and total mass flux defined in Eq. (26)	kg m ⁻² s ⁻¹ , Kg m ⁻¹ s ⁻¹
R^*	equivalent particle radius between two contacting particles	m
Re_p	particle Reynolds number	1
S_i, S_j	contact area of particle i and j	m ²
\vec{u}_r	particle-to-wind relative velocity	m s ⁻¹
u_m	mean streamwise wind speed	m s ⁻¹
u_*	friction velocity	m s ⁻¹

Table 1. Continued.

Symbols	Physical meaning	Units
$\vec{u}_{p,i}$	velocity of particle i	m s^{-1}
$u_{p,i}, w_{p,i}$	streamwise and vertical components of particle velocity	m s^{-1}
$\langle u_p \rangle$	mean particle horizontal speed	m s^{-1}
v_{imp}	impact speed of the saltating particle	m s^{-1}
$\vec{v}_{ij}, \vec{v}_{ij}^n, \vec{v}_{ij}^t$	relative velocity between particle i and j at the contact point, and its normal and tangential components	m s^{-1}
\vec{x}_i, \vec{x}_j	position vectors of particle i and j	m
$Y=10^8$	Young's modulus of particles	Pa
Y^*	equivalent Young's modulus between two contacting particles	Pa
z, z^*	height above the ground and dimensionless height	m, 1
z_0	the aerodynamic roughness	m
z_{salt}	saltation height	m
β	damping coefficient of collisional forces	1
$\gamma_s=0.5, \gamma_r=0.1$	coefficients of static and rolling friction	1
$\zeta_{p,i}$	charge-to-mass ratio of particle i	C kg^{-1}
η_n	residual of EEMD or EMD	-
θ, φ	rebouncing angles of particles	$^\circ$
$\kappa \approx 0.41$	von Kármán constant	1
τ_p	particle momentum flux	Pa
$\vec{\omega}_{p,i}$	angular velocity of the particle i	rad s^{-1}
δ_n, δ_t	normal and tangential overlap between two contacting particles	m
$\mu=1.8 \times 10^{-5}$	dynamic viscosity of the air	$\text{Pa}\cdot\text{s}$
$\nu=0.3$	Poisson's ratio of particles	1
ξ_i	EEMD component or IMF of EMD	-
$\rho_a=1.174$	air density	kg m^{-3}
$\rho_p=2650$	particle mass density	kg m^{-3}
ρ_c	space charge density	C m^{-3}
ρ_h^i, ρ_h^j	density of the electrons trapped in the high energy states on the surface of particle i and j	m^{-2}
σ	surface charge density	C m^{-2}
σ_p	geometric standard deviation of particle sample in the numerical model	1
χ_N	the i -th level wavelet detail component	-
ψ_i	the N -th level wavelet approximation component	-
Δq_{ij}	net increment of the charge of particle i after colliding with particle j	C
Δz	vertical grid size	m

1

2

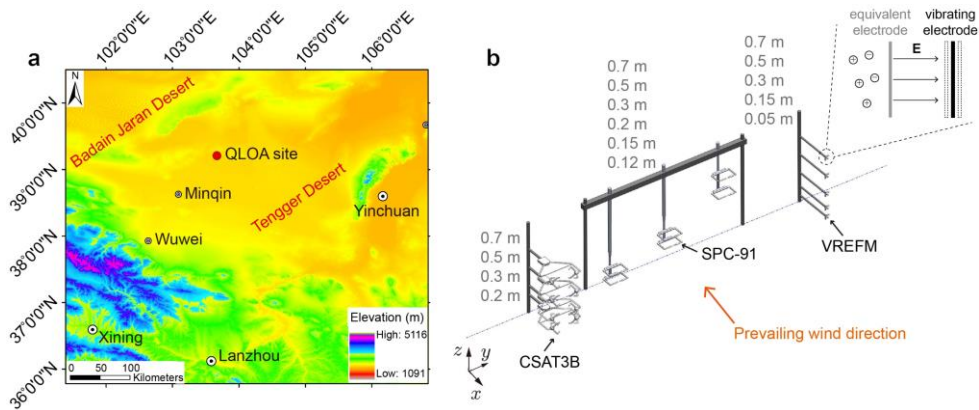
1 **Table 2.** Fitting coefficients of the 3-order polynomial curves in Fig. 6.

Components	$a_{0,i}$	$a_{1,i}$	$a_{2,i}$	$a_{3,i}$	R^2
$i = 1$	-2.17	4.02	-2.24	0.31	0.97
$i = 2$	-0.71	2.06	-1.49	0.23	0.80
$i = 3$	0.55	-1.41	1.24	-0.21	0.67

2

3

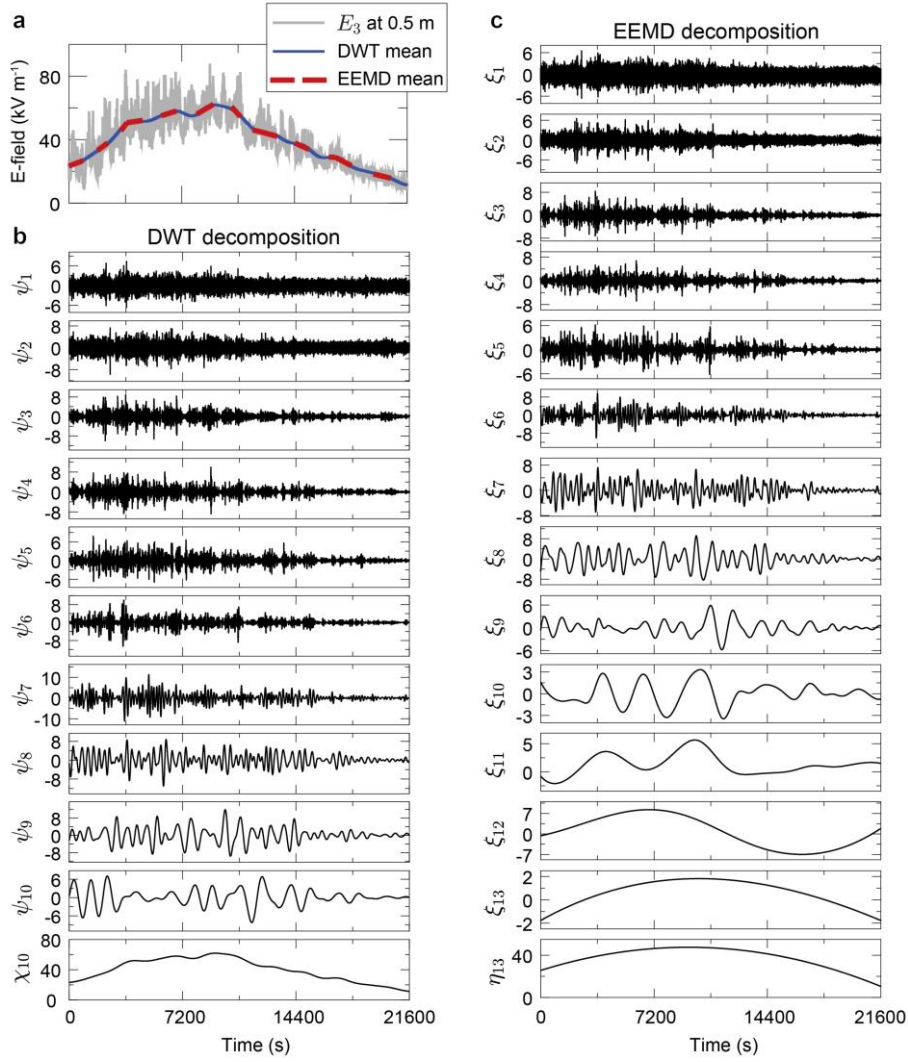
1



2

3 **Figure 1.** Map of the QLOA site and the layout of all instruments. (a) The QLOA site is
4 located between the Badain Jaran Desert and the Tengger Desert, approximately 90
5 km northeast of Minqin, Gansu, China. (b) Four CSAT3B sensors were mounted at 0.2-
6 0.7 m height, respectively; six SPC-91 sensors were mounted at 0.12-0.7 m height,
7 respectively; total fifteen VREFM sensors were mounted to measure the 3-D E-field at
8 0.05-0.7 m height, respectively (that is, at each measurement point, three VREFM
9 sensors are mutually perpendicular). The CSAT3B, SPC-91, and VREFM sensors were
10 distributed along a straight line parallel to the y axis, and the prevailing wind
11 direction in the QLOA site is parallel to the x axis. The inset shows the working
12 principle of the VREFM, where the charged particles and the vibrating electrode forms
13 a dynamic capacity.

14



2

3 **Figure 2.** The resulting DWT and EEMD components from a measured vertical E-field4 component E_3 at 0.5 m height, with a total of $N_d=21600$ data points. Panel (a) shows

5 the original E-field time series (gray line), as well as the time-varying mean obtained

6 by DWT (blue line) and EEMD (red dashed line). Panel (b) shows the detailed

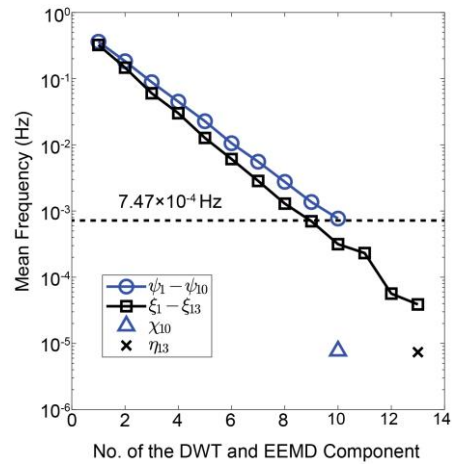
7 components ψ_1 - ψ_{10} and approximation component χ_{10} of DWT. Panel (c) shows8 the EEMD components ξ_1 - ξ_{13} and the residue η_{13} . In the EEMD, N is specified as9 $\log_2(N_d) - 1$, the member of the ensemble N_e is 100, and the added white noise in

10 each ensemble member has a standard deviation of 0.2. Times are shown relative to

11 May 6, 2014 at 13:00:00 UTC+8.

12

1



2

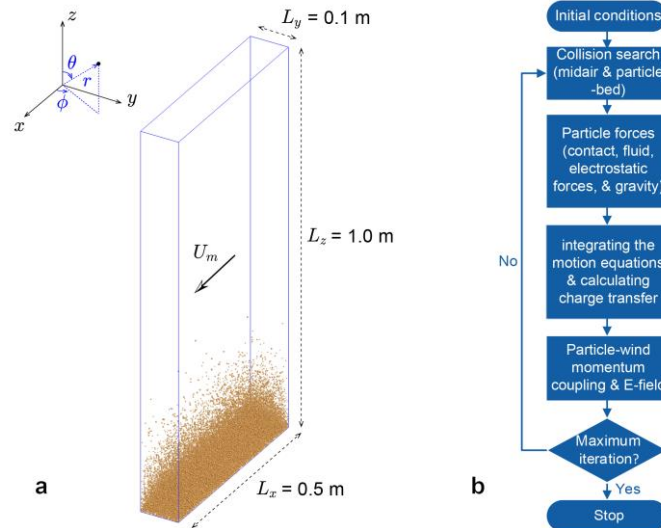
3 **Figure 3.** The Mean frequencies of DWT and EEMD components of E_3 at 0.5 m height.

4 The dashed line around the components ψ_{10} and ξ_9 corresponds to the frequency

5 of 7.47×10^{-4} Hz.

6

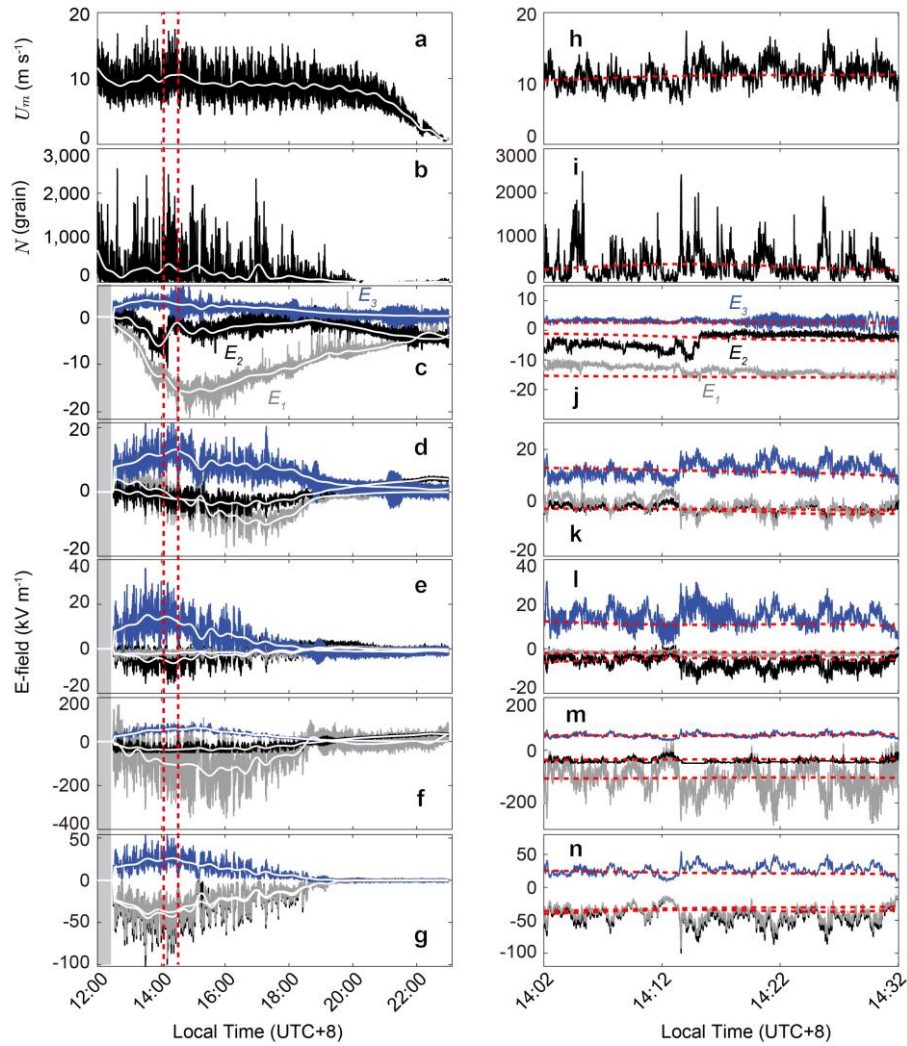
1



2

3 **Figure 4.** A schematic illustration of the DEM simulation of saltation and the numerical
4 algorithm of the saltation model. (a) A 3-D view of the simulated wind-blown sand at
5 the steady-state, where the wind shear velocity $u_* = 0.5 \text{ m s}^{-1}$, average sand diameter
6 $d_m = 228 \text{ }\mu\text{m}$, and geometric standard deviation $\sigma_p = \exp(0.3)$. Both the Cartesian and
7 spherical coordinates are shown in the inset. (b) This flowchart shows the scheme for
8 simulating the saltation according to the following steps implementing the DEM with
9 particle triboelectric charging: initial conditions, collision search, particle forces,
10 integrating motion equations and calculating charge transfer, particle-wind
11 momentum coupling and evaluating E-field, and finally repeating these execute steps
12 until reaching the maximum iteration steps.

13



1

2 **Figure 5.** Measured data during a dust storm occurring on May 6, 2014, at the QLOA
 3 site. Panels (a)-(b) show the measured time series of the streamwise wind speed, u_m

4 at 0.7 m and the number of saltating particle N at 0.15 m. Panels (c)-(g) correspond

5 to the streamwise E-field E_1 (grey lines), spanwise E-field E_2 (black lines), and
 6 vertical E-field E_3 (blue lines) at 0.05, 0.15, 0.3, 0.5, and 0.7 m height, respectively.

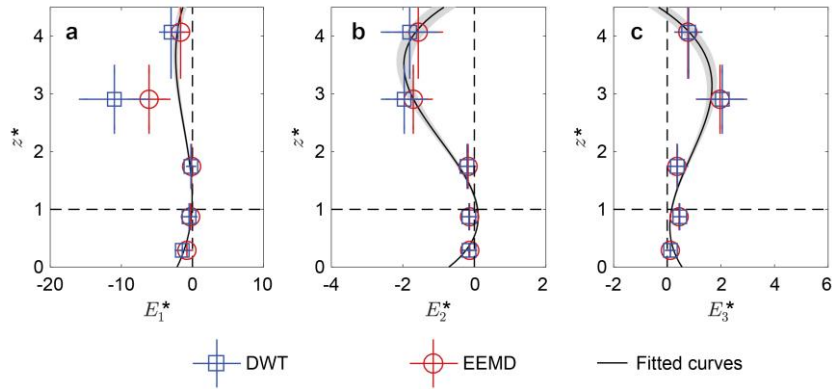
7 Unfortunately, owing to the interruption of power supply, the 3-D E-field data have not
 8 been recorded before $\sim 12:30$, as represented by a shaded area in the last five panels

9 (c)-(g). The dashed box denotes the relatively stationary period of the observed dust
 10 storm because during this period the time-varying means of all quantities (such as χ_{10}

11 depicted by the solid white lines in panels a-g and dashed red lines in panels h-n) do
 12 not vary notably as time varies (Bendat and Piersol, 2011), as shown in (h)-(n).

13

1



2

3 **Figure 6.** Vertical profiles of the normalized 3-D E-field. Panels (a)-(c), in turn,
4 correspond to the vertical profiles of E_1^* , E_2^* , and E_3^* of the observed dust storm.

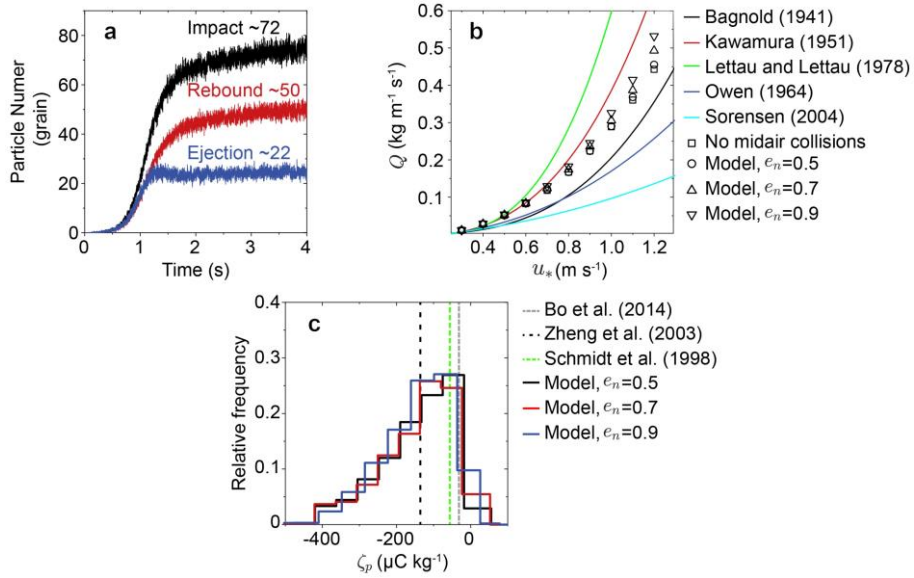
5 Squares and circles denote the DWT mean and EEMD mean values of the normalized
6 E-field data, respectively. Error bars are standard deviations. Lines denote robust linear

7 least-squares fitting of the normalized E-field data obtained by DWT and EEMD
8 method using 3-order polynomials (with R^2 of 0.97, 0.80, and 0.67, respectively),

9 where the shaded areas denote 95% confidence bounds.

10

1



2

3 **Figure 7.** Verification of the steady-state numerical model in the case of pure saltation.

4 That is, only vertical E-field needs to be considered, which is produced by the charged

5 saltating particles. (a) The number of the impacting, rebounding, and ejected particles

6 within each period of 10^{-4} s, where $u_* = 0.5$ m s $^{-1}$, $d_m = 228$ μ m, and $\sigma_p = \exp(0.3)$. (b)

7 Comparison of the simulated total mass flux with the most commonly-used

8 semiempirical saltation mass flux equations (Bagnold, 1941; Kawamura, 1951; Lettau

9 and Lettau, 1978; Owen, 1964; Sørensen, 2004), where $d_m = 228$ μ m, and $\sigma_p = \exp$

10 (0.3). (c) Comparison of the simulated charge-to-mass ratio distribution in the range

11 of 0.07-0.09 m height with the measured mean charge-to-mass ratio, in the range of

12 0.06-0.1 m height (Zheng et al., 2003), at 0.05 m height (Schmidt et al., 1998) and 0.08

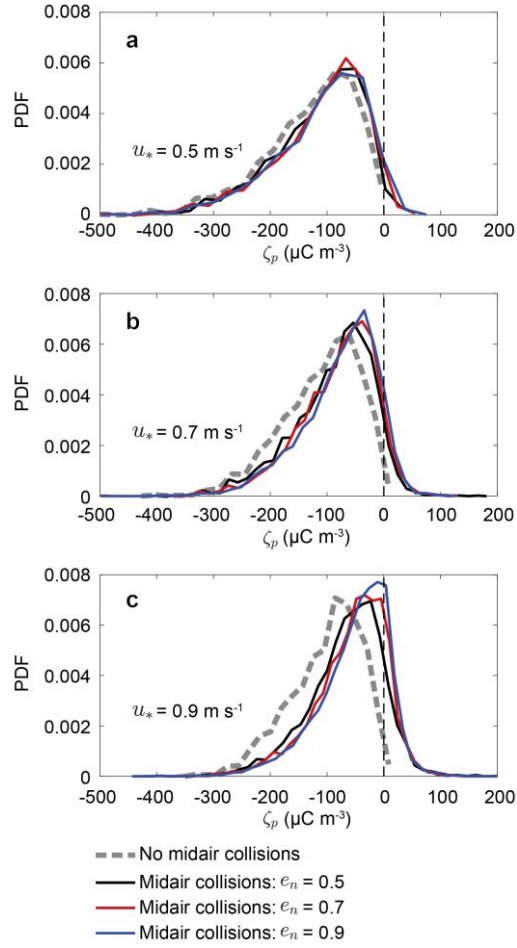
13 m height (Bo et al., 2014). Here, $\rho_h^0 = 6 \times 10^{15}$ m $^{-2}$ is determined by calibrating the model

14 with measurements; $u_* = 0.35$ m s $^{-1}$, $d_m = 203$ μ m, and $\sigma_p = \exp(0.33)$ are estimated

15 from (Zheng et al., 2003).

16

1

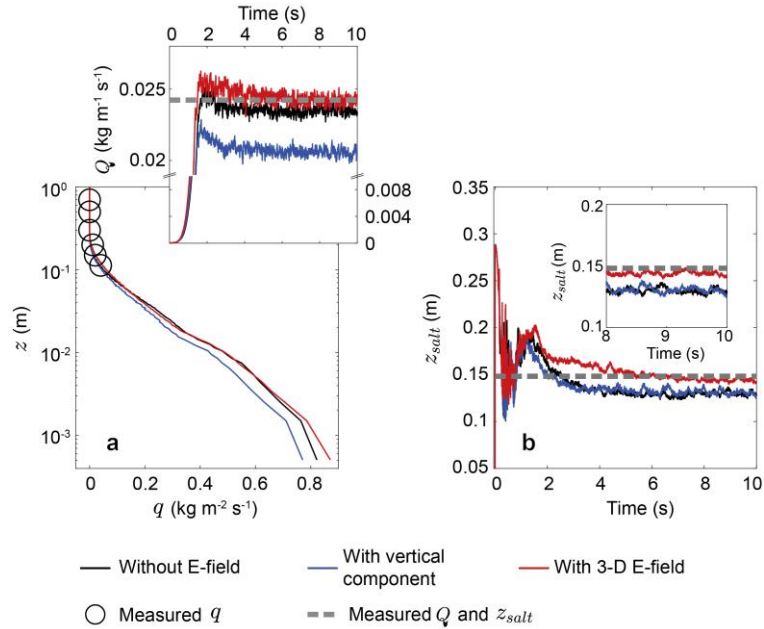


2

3 **Figure 8.** Effects of midair collisions on the probability density function (PDF) of charge-
 4 to-mass ratio of saltating particles for various wind velocities (a) $u_* = 0.5 \text{ m s}^{-1}$, (b)
 5 $u_* = 0.7 \text{ m s}^{-1}$, and (c) $u_* = 0.9 \text{ m s}^{-1}$, where $d_m = 203 \text{ }\mu\text{m}$, $\sigma_p = \exp(0.33)$, and $\rho_h^0 = 6 \times 10^{15}$
 6 m^{-2} .

7

1

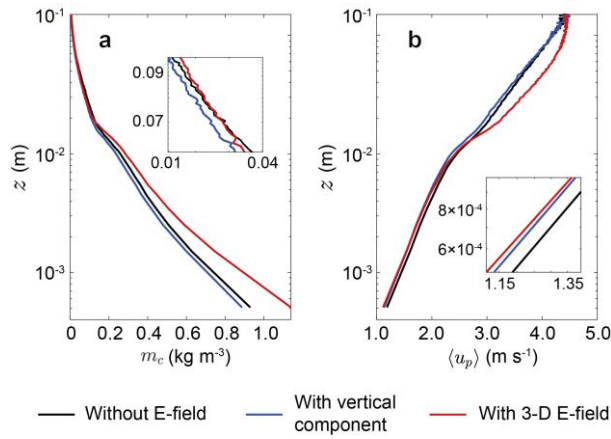


2

3 **Figure 9.** Comparison of the simulated mass flux q and total mass flux Q (a) and
 4 saltation height z_{salt} (b) with our measurements in the relatively stationary period of
 5 the observed dust storm (shaded areas in Fig. 4 and Fig. S3 in the Supplement), where
 6 $u_* = 0.37 \text{ m s}^{-1}$, $d_m = 200 \text{ }\mu\text{m}$, $\sigma_p = \exp(0.42)$, $\rho_h^0 = 6 \times 10^{15} \text{ m}^{-2}$, and $e_n = 0.7$. (a) Circles
 7 are the measured mean mass flux, dashed line denotes the estimated mean total mass
 8 flux, and lines denote the simulated results. (b) Dashed lines denote the estimated
 9 saltation height based on our measurements and lines denote simulated results. Inset
 10 shows the same data from 8 to 10 s. The uncertainty analysis of the measured or
 11 estimated results can be found in Text S1 in the Supplement.

12

1

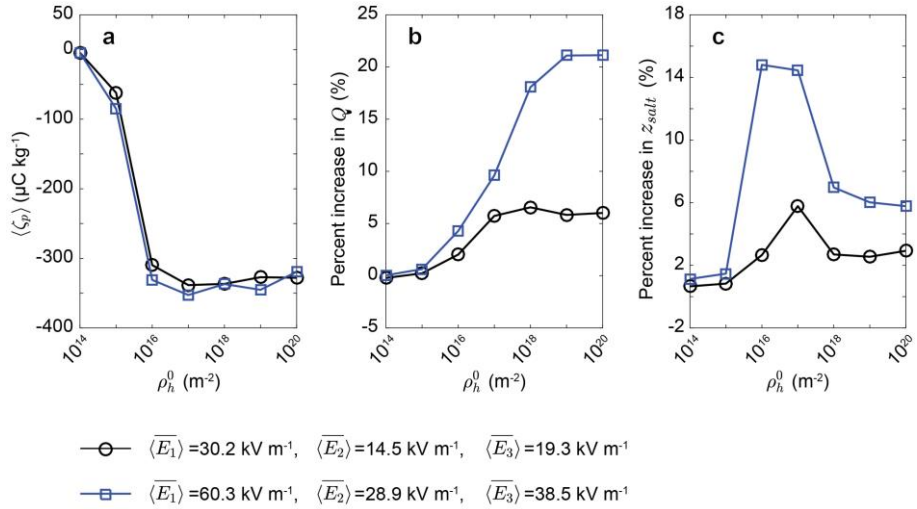


2

3 **Figure 10.** Vertical profiles of the particle mass concentration m_c and mean particle
4 horizontal speed $\langle u_p \rangle$ for different cases, where $\langle u_p \rangle$ is calculated as the arithmetic
5 mean of particle horizontal speed located in the range of $[z, z + \Delta z]$. Insets show the
6 same data and emphasize the local information. In these cases $u_* = 0.37 \text{ m s}^{-1}$,
7 $d_m = 200 \text{ }\mu\text{m}$, $\sigma_p = \exp(0.42)$, $\rho_h^0 = 6 \times 10^{15} \text{ m}^{-2}$, and $e_n = 0.7$.

8

1



2

3 **Figure 11.** Effects of the density of charged species ρ_h^0 on saltation for two different
 4 height-averaged time-varying mean levels (i.e. $\langle \bar{E}_i \rangle$, $i = 1,2,3$). (a) The mean charge-
 5 to-mass ratio $\langle \zeta_p \rangle$ (in the range from 0.07 to 0.09 m height) as a function of ρ_h^0
 6 ranging from 10^{14} to 10^{20} m^{-2} (e.g. Kok and Lacks, 2009). (b) Percent increase in the
 7 total mass flux Q as a function of ρ_h^0 . (c) Percent increase in the saltation height z_{salt}
 8 as a function of ρ_h^0 . The squares correspond to the height-averaged time-varying
 9 mean in the stationary stage of the observed dust storm (shaded areas in Fig. S7 in the
 10 Supplement). In these cases, $e_n=0.7$.